B. Haanen

MSc. Thesis

A MATE for post-stroke gait rehabilitation; design optimization of a minimally actuated tendon-based gait rehabilitation device

A MATE for post-stroke gait rehabilitation; design optimization of a minimally actuated tendon-based gait rehabilitation device

By

B. Haanen

in partial fulfilment of the requirements for the degree of

Master of Science
in Mechanical Engineering

at the Delft University of Technology,
to be defended on Thursday August 26, 2021 at 14:30.

Supervisors:	Prof. dr. ing. L. Marchal-Crespo,	
	Prof. dr. ing. H. Vallery.	
Thesis committee:	Prof. dr. ing. L. Marchal-Crespo,	TU Delft
	Prof. dr. ing. H. Vallery,	TU Delft
	Dr. ir. E. van der Kruk,	TU Delft
	Prof. dr. ir. J. Harlaar.	TU Delft

PREFACE

When starting this master thesis six months ago, I expected a project in which I could further hone my existing strengths. I planned to design and build a robot using my knowledge of dynamics, my practical skills and evaluate this model with extensive tests and statistical analyses. Instead of honing these existing skills, I developed a whole new set of skills and knowledge. From carefully evaluating all possibilities to researching existing literature for additional methods, knowledge, and data. For this I am very grateful, as I believe these new skills are important, and this process has made me more complete as an engineer.

I started this project with very limited knowledge about optimizations and created an extensive double-loop optimization. Furthermore, the existence of tendon-based robots was practically unknown to me before starting this project. I learned a lot about the strengths and working principles of these robots. Moreover, I learned about the complexity of overactuation in robots and how to work in different spaces using Jacobians. Lastly, I have always felt that my MATLAB skills were not on par with my fellow students. I have primarily worked in MATLAB for this thesis, which developed my skills and let me catch up to my peers.

I'm very grateful to Laura Marchal-Crespo for giving me this opportunity and to Heike Vallery for jumping in without hesitation to become co-supervisor of the project. I want to thank them both for their guidance during this project, pointing me in the right direction when needed while giving me enough freedom to make decisions about the project and figure things out myself.

Furthermore, I would like to thank Jesper Kreuk for his technical insights, Laurence Koopman for always listening and thinking along, and Raphael Raetz for his insights in the optimization. Lastly, I'd like to thank Jacqueline de Hoog for always being there for me and cheering me up when needed.

CONTENTS

A MATE for post-stroke gait rehabilitation; design optimization of a minimally actuated tendon-based gait rehabilitation device

Bram Haanen

Abstract—**Robots can be powerful tools in post-stroke gait rehabilitation. However, state-of-the-art robots are often expensive machines containing rigid links with high inertia. Their expensiveness could limit their availability, and their high inertia reduces transparency, which could hinder rehabilitation progress. These factors raise the need for a minimalistic transparent robot that can effectively fill this gap. This research aims to design and validate such a device, a minimally actuated tendon-based exercise environment. The device is synthesized using an optimization algorithm that considers possible system configurations and optimizes both these configurations and their respective design parameters. Validation is done based on a reconstructed simulation of gait using motion capture on the optimal design to check whether it could be used for real-life rehabilitation. It was found that the most simplistic solution is not yet adequate for rehabilitation; thus, a slightly more complex design is required. While not providing the final solution, this research provides an important stepping stone towards designing a minimally actuated, simplistic, and transparent rehabilitation device.**

I. INTRODUCTION

Stroke is the third leading cause of disabilities worldwide [1]. This is not surprising, given the fact that about 13.7 million stroke occurrences are reported worldwide, every year [2]. Most of the survivors are left with sensorimotor disabilities, which are severe enough to leave 2 out of 3 patients without independent walking ability [3]. Significant improvements in gait function can be made with rehabilitation, as shown by review papers [4]–[7]. The most vital improvements in gait function are made during the first 11 weeks after a stroke [3]. These early stages are thus critical in the overall rehabilitation process, emphasising that patients should receive sufficient and effective therapy during this time.

While conventional post-stroke gait rehabilitation has proven its effectiveness by improving gait function [4], [5], [7], the availability of therapy during the critical early stages following stroke could be increased. Assisting patients suffering from post-stroke disabilities can be labour intensive for therapists [8], as it requires the therapists to physically support the patient and assist the movement of the paretic leg [9]. Up to three therapists could be required to assist a patient walking on a treadmill [10]. This limits the availability of therapists, which limits therapy intensity, which is crucial for effective rehabilitation. Robotic solutions could relieve therapists, taking over the labour-intensive aspects, and thus, reduce the existing limits on therapy intensity [11].

Because robots are promising prospects for gait rehabilitation, the research field of rehabilitation robotics has been rapidly growing and evolving over the last 20 years. Many prototypes and commercial products emerged during this time [11]–[13]. Previous research has already indicated rehabilitation robots can significantly improve gait function when used in conjunction with conventional rehabilitation, as shown by review papers [11], [14].

Although state-of-the-art rehabilitation robots are potent, they do still suffer from two major intrinsic drawbacks. Firstly, they commonly are heavy, high inertia systems. Adding inertia to the leg movement produces additional unwanted forces during gait, decreasing transparency [8]. Transparency indicates the degree to which unwanted interaction forces between the subject and robot are present [15], where low transparency can be detrimental to the effectiveness of gait rehabilitation [8]. This inertia effect could be partially compensated with control strategies using gravitational compensation; however, some inertia residue will always remain [16]. The second drawback is that rehabilitation robots can be highly sophisticated, and thus, expensive. The Lokomat (Hocoma AG, Switzerland), a state-of-the-art gait rehabilitation exoskeleton, costs around €330,000.00, with annual maintenance costs being around 10% of the initial purchase cost [17]. These high prices limit their availability, especially in less developed countries.

Robot transparency could be increased by tendon-based robots, as they are intrinsically lightweight, consisting of only tendons and winches [18]. Some early research has already been conducted on these robots with both exoskeletons [19] and end-effectors [20]. Some preliminary research already indicates the effectiveness of tendon-based robots in rehabilitating gait function [21]–[23]. However, state-of-the-art tendon-based robots are still very sophisticated robots consisting of many components, which could indicate expensiveness. This second drawback of state-of-the-art gait rehabilitation robots, expensiveness, could be improved by striving for minimal actuation. This could reduce the number of motors, sensors, and power required, which would lessen costs. Importantly, minimal actuation also has some additional benefits. It simplifies ensuring subject safety, as less powerful motors are used [18]. Furthermore, it encourages patients' active participation, which is crucial in neurorehabilitation [24].

Based on the clinical need for a transparent and affordable gait rehabilitation robot, the Minimally Actuated Tendon-based Exercise environment (MATE) has been developed. Transparency is increased by using tendons instead of rigid links. Affordability is achieved by striving for minimal actuation. Stroke patients are often hemiparetic [25], i.e. disabled on one side of the body. This implies that the assisting forces can be provided by the non-paretic leg, requiring only the minimal actuation provided by the treadmill. Therefore, MATE connects both legs via tendons, effectively creating an end-effector type "robot", with a possible design displayed in Figure 1. This approach has to our knowledge, not been researched yet. Therefore, it is unknown whether connecting the legs alters the gait pattern by producing unwanted, parasitic forces. This research aims to determine whether the legs can be directly connected such that MATE does not alter a normal gait pattern, i.e. checking whether only minimal parasitic forces are produced during healthy gait.

Achieving this aim requires an optimal design, which is validated against forces known to alter healthy gait. Multiple potential configurations were systematically determined and used in conjunction with gait data from six healthy subjects to create a simulation of subjects using MATE. This simulation was used to optimize both the configuration and its respective design parameters on four out of six healthy subject simulations. The best performing of these designs was chosen as the optimal design, for which the parasitic forces were evaluated against force thresholds known increase step length on the two remaining subject simulations.

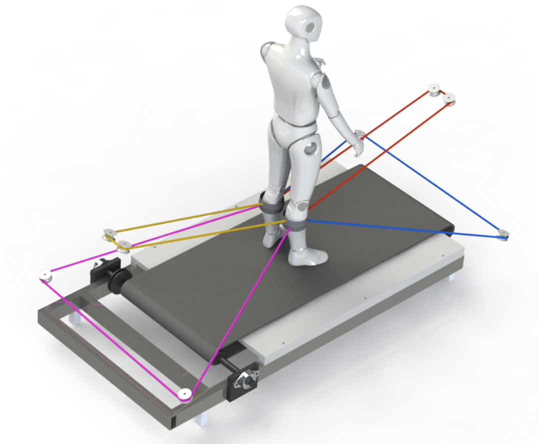

Fig. 1: Overview of the MATE robot on a subject. MATE connects both legs via a total of four tendons, each given a different color here for clarity.

II. METHODS

A. Possible configurations for MATE

The design of MATE mimics an end-effector type robot by directly connecting tendons to the legs without any orthoses. This approach is selected as it further reduces the mass on the legs, compared to exoskeleton type robots that require orthoses [13]. Moreover, using orthoses could also further increase the cost of MATE. Tendons are connected to a single cuff per leg to reduce mass and cost even further.

The assumption that the tendons connect to a single point on each leg was taken for further calculations, as the cuffs' dimensions are small. This assumption implies that only translational control of the x-, y-, and z-position is possible, i.e. three Degrees of Freedom (DoF) per leg. A drawback of tendons is that they can only provide tension forces, and therefore tendon-based robots often require over-actuation [26]. MATE also suffers from this drawback, requiring four tendons at each leg to control the three translation DoF, as shown in Figure 1.

To find the optimal design for MATE, a systematic approach was used to find as many of the potential system configurations as possible. The robot has identical working principles on both sides of the coronal plane, i.e. the front and back of the subject, so only one side was checked for potential tendon configurations. The resulting configurations were evaluated for both sides. The first step of the systematic search was finding the total number of available configurations $n_{\mathrm{c,t}}$. This relies on the number of pulleys n_{p}, the pulleys used per tendon $n_{\mathrm{p,t}}$, and the number of possible pulley configurations $n_{\mathrm{p,c}}$. Their relation is defined by Equation 1:

$$n_{\mathrm{c,t}} = \frac{n_{\mathrm{p}}!}{n_{\mathrm{p,t}}} n_{\mathrm{p,c}}. \tag{1}$$

The second step of the systematic search was defining all $n_{\mathrm{c,t}}$ potential configurations and evaluating them on two feasibility criteria. These criteria are that configurations must allow for full control of all three DoF and that configurations should not result in tendon collisions during normal use. The configurations that satisfy these criteria, C_i, will subsequently be used to determine the optimal design. Appendix A contains a more detailed explanation about the systematic search and these feasibility criteria.

B. Obtaining and pre-processing of gait data

MATE is designed to stimulate a healthy gait pattern, and thus, it is both optimized and validated on healthy gait data. Therefore, marker position recordings from 6 healthy subjects during free treadmill walking were used. This data was provided by Saher Jabeen from yet to be published work. The markers used to recreate the gait in a simulation with MATLAB (R2021b, Mathworks) are shown in Figure 2. The reasoning behind this marker placement is explained in Appendix B. Subjects were reconstructed in simulation using the FMH markers to represent the hips, the average of FLE and FME for the knees, and the middle of MM and LM for the ankles. Subjects ranged from 23 to 30 years old, four were male and two female, and ranged between 155 cm to 186.5 cm in height and 51 kg to 72.5 kg in mass. A full overview of the demographic and anthropomorphic information of all subjects is shown in Table II. These ranges provide a potential spread of healthy gait patterns, useful for evaluating the designs for general implementation, i.e. the use on different patients.

The obtained data was collected using a system of 12 infrared motion tracking cameras (Oqus 700, Qualisys, USA) at 100 Hz. The left heel marker (L_CAL) was used to determine heel strikes used to detect gait cycles. A sequence of 10 gait cycles was substracted during steady gait at an arbitrarily chosen point from each subject. One issue upon analyzing this data was that subjects tend to drift both in the coronal and sagittal direction during free treadmill walking. Since presumably, MATE will centre subjects, this drift was removed. The drift was identified with a third-order low pass filter on the left hip marker (L_FMH) with a cutoff frequency at $w_{\mathrm{c}} = 0.5\,\mathrm{Hz}$, and was subsequently subtracted from all marker points shown in Figure 2. The filter was used in both the forward and reverse direction to avoid phase shift. The cutoff frequency was iteratively determined to capture the drift but avoid intra-step variability by visually inspecting the filtered and processed data. The intra-step variability was kept as it is relevant to the evaluation of MATE since this variability can also be expected during actual use of MATE. The full process from marker data to a reconstructed simulation is explained in detail in Appendix B.

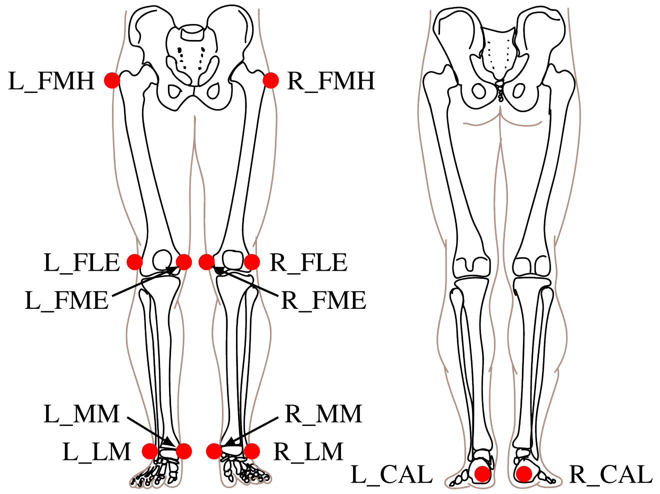

Fig. 2: Marker positions used during motion capture by Saher Jabeen. The shown markers were used to simulate the subjects' gait. The front view of the subject is shown on the left and the back view on the right.

C. *Finding the optimal design*

1) *Cost function*

The cost function is the key determinant in achieving the objective of the design process, and should therefore capture a relevant metric. In this case, a relevant metric to evaluate for a healthy subject are the parasitic forces acting on the legs, i.e. the undesired forces that occur during a healthy trajectory. Therefore, the cost function should be focused on minimizing these forces. Since the gait data was obtained from healthy participants, their gait trajectory was assumed to be the ideal trajectory for them. All forces acting on their legs during this ideal trajectory are, thus, undesired parasitic forces. The forces on the left leg are represented by $F_{\mathrm{L,x}}, F_{\mathrm{L,y}}$ and $F_{\mathrm{L,z}}$ in the x-, y-, and z-direction respectively. In the same order the forces on the right leg are represented by $F_{\mathrm{R,x}}, F_{\mathrm{R,y}}$ and $F_{\mathrm{R,z}}$. These forces can have both positive and negative values, and thus the sum of the root mean squared error ($RMSE$) of all these forces is chosen as the cost function

$$\begin{aligned}\psi = \mathrm{RMSE}(F_{\mathrm{L,x}}) + \mathrm{RMSE}(F_{\mathrm{L,y}}) + \mathrm{RMSE}(F_{\mathrm{L,z}}) + \\ \mathrm{RMSE}(F_{\mathrm{R,x}}) + \mathrm{RMSE}(F_{\mathrm{R,y}}) + \mathrm{RMSE}(F_{\mathrm{R,z}}).\end{aligned} \tag{2}$$

Parasitic forces occur because movement during the stance and swing phase of the legs is not fully symmetrical, and one leg is often in swing phase while the other is in stance phase. Because of this, the tendon length might not be constant, and could slightly fluctuates during a gait cycle. Forces in the tendons $\vec{F_{\mathrm{t}}}$ are thus produced by the tendon length deviations $\vec{u_{\mathrm{t}}}$ and tendon stiffness k_{t} with

$$\vec{F_{\mathrm{t}}} = k_{\mathrm{t}} \vec{u_{\mathrm{t}}}. \tag{3}$$

The forces in Cartesian space on the legs $\vec{F_{\mathrm{L}}}$ and $\vec{F_{\mathrm{R}}}$ are more relevant to the user than tendon forces $\vec{F_{\mathrm{t}}}$, as the user will directly experience the Cartesian forces. Therefore, the Cartesian forces are used in the cost function. To calculate Cartesian forces, tendon forces are mapped to the Cartesian space as follows:

$$\vec{F_{\mathrm{L}}} = {\mathbf{J}_{\mathrm{t,L}}}^T \vec{F_{\mathrm{t}}}, \tag{4}$$

$$\vec{F_{\mathrm{R}}} = {\mathbf{J}_{\mathrm{t,R}}}^T \vec{F_{\mathrm{t}}}. \tag{5}$$

Here ${\mathbf{J}_{\mathrm{t,L}}}^T$ and ${\mathbf{J}_{\mathrm{t,R}}}^T$ are the Jacobians from Tendon to Cartesian space, for the left and right leg respectively. Equations 4 and 5 are derived using singular values in Appendix C. The required Jacobians can be calculated with the inverse kinematics, i.e. deriving the tendon lengths to the Cartesian coordinates,

$$\mathbf{J}_{\mathrm{t}} = \begin{pmatrix} \frac{\partial L_1}{\partial x} & \frac{\partial L_1}{\partial y} & \frac{\partial L_1}{\partial z} \\ \frac{\partial L_2}{\partial x} & \frac{\partial L_2}{\partial y} & \frac{\partial L_2}{\partial z} \\ \frac{\partial L_3}{\partial x} & \frac{\partial L_3}{\partial y} & \frac{\partial L_3}{\partial z} \\ \frac{\partial L_4}{\partial x} & \frac{\partial L_4}{\partial y} & \frac{\partial L_4}{\partial z} \end{pmatrix}, \tag{6}$$

with L_i representing the length of tendon $i = 1, .., 4$. A more extensive derivation of Equation 6 can be found in Appendix C. Using the Cartesian coordinates of the left leg $x_{\mathrm{L}}, y_{\mathrm{L}}$ and z_{L} in Equation 6 results in ${\mathbf{J}_{\mathrm{t,L}}}^T$ and the coordinates of the right leg $x_{\mathrm{R}}, y_{\mathrm{R}}$ and z_{R} gives ${\mathbf{J}_{\mathrm{t,R}}}^T$.

The tendon stiffness k_{t} in Equation 3 was obtained by evaluating results of adaptive impedance stiffness tests with spinal cord injury patients in ARTHuR [27], and healthy subjects and a single spinal cord injury patient in Lokomat [28]. ARTHuR is an end-effector robot using forcer coils, and Lokomat is a state-of-the-art exoskeleton which uses impedance control. While their results vary between subjects and during different phases of the gait cycle, they can be used to generate a safe and high stiffness estimate. If the parasitic forces are minimal with this high stiffness, it can be assumed that no tendon length compensation is required. Based on this assumption and the impedance stiffness after convergence for ARTHuR [27] and Lokomat [28], a horizontal stiffness of $k_{\mathrm{xx}} = 1\,\mathrm{kN/m}$ was selected for validation. This estimate followed from a visual inspection of the graphs reported in both studies. However, stiffness k_{xx} is in the Cartesian space, while stiffness k_{t} in Equation 3 is in Tendon space. The stiffness k_{xx} is a part of the Cartesian stiffness matrix $\mathbf{K_x}$, whose relation with k_{t} is determined by the Jacobian $\mathbf{J}_{\mathrm{t}}$ [29],

$$\mathbf{K_x} = {\mathbf{J}_{\mathrm{t}}}^T k_{\mathrm{t}} \mathbf{J}_{\mathrm{t}}. \tag{7}$$

Extra information and proof in singular values of Equation 7 is described in Appendix B. Because only the horizontal stiffness k_{xx} is taken as a reference, this component can be extracted from equation 7, which gives

$$k_{\mathrm{t}} = \left(\left(\frac{\partial L_1}{\partial x}\right)^2 + \left(\frac{\partial L_2}{\partial x}\right)^2 + \left(\frac{\partial L_3}{\partial x}\right)^2 + \left(\frac{\partial L_4}{\partial x}\right)^2 \right)^{-1} k_{\mathrm{xx}}. \tag{8}$$

2) *Parameters and bounds*

The optimization algorithm optimizes a set of parameters for each feasible configuration from C_i based on cost function ψ. The parameters to optimize for each C_i are

$\vec{p}_j = \begin{bmatrix} w_1 & z_1 & w_2 & z_2 & w_3 & z_3 & w_4 & z_4 \end{bmatrix}$, whose definitions are visualized in Figure 3. The pulleys were fixed at $0.75\,\mathrm{m}$ in front and behind the subject, i.e. the positive and negative x-direction, assuming a treadmill length of $1.5\,\mathrm{m}$. The optimal design of MATE is the configuration and parameter set with the lowest cost function value. Upper and lower bounds constrained the optimization on the parameters to ensure the system maintains full control of all three translational DoF per leg by forcing tendons to point towards the required directions. This was checked with a visual inspection of the simulation. Furthermore, the bounds were chosen to increase both patient and therapist safety in case of cables snapping by always being below hip height. The parameter bounds for each C_i are tabulated in Table I. The initial parameter estimates were set at the average of each lower and upper bound.

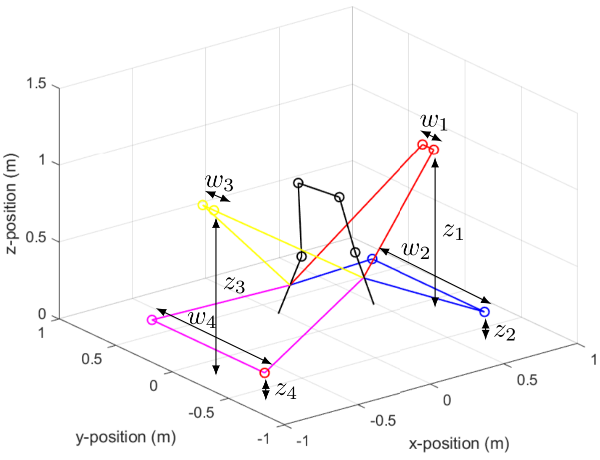

Fig. 3: Simulation of MATE in configuration one with subject one. The eight design parameters for the optimization are also visualized here.

	w_1	z_1	w_2	z_2	w_3	z_3	w_4	z_4
$C_{1,\mathrm{low}}$ (m)	0	0.5	0.2	0.1	0	0.5	0.2	0.1
$C_{1,\mathrm{up}}$ (m)	0.05	1.0	0.4	0.3	0.05	1.0	0.4	0.3
$C_{2,\mathrm{low}}$ (m)	0.2	0.5	0	0.1	0.2	0.5	0	0.1
$C_{2,\mathrm{up}}$ (m)	0.4	1.0	0.05	0.3	0.4	1.0	0.05	0.3
$C_{3,\mathrm{low}}$ (m)	0	0.5	0.2	0.1	0	0.5	0.2	0.1
$C_{3,\mathrm{up}}$ (m)	0.05	1.0	0.4	0.3	0.05	1.0	0.4	0.3
$C_{4,\mathrm{low}}$ (m)	0.2	0.5	0	0.2	0.1	0.5	0	0.1
$C_{4,\mathrm{up}}$ (m)	0.4	1.0	0.05	0.4	0.5	1.0	0.05	0.3

TABLE I: Upper and lower bounds for all configurations. The lower bound of configuration i is given by $C_{i,\mathrm{low}}$, and the upper bound by $C_{i,\mathrm{up}}$.

3) *Optimization algorithm*

The selection of the optimization algorithm is a crucial factor in minimizing the parasitic forces of MATE's final design. In total, eight parameters are optimized over four different configurations for four subjects. Due to many parameters and optimizations, the potential presence of multiple local minima was checked. This was done by varying one parameter at a time and evaluating the cost function value against this parameter, the results which are shown in Appendix C. This process revealed that the cost function indeed has multiple local minima, which warrants the need to use a global optimization method [30]. A genetic algorithm is selected for the optimization of MATE. Genetic algorithms mimic evolution theory [31] by using offspring to converge towards possible solutions and mutations to escape local minima [30]. These properties make genetic algorithms a good fit for the optimization of MATE.

The genetic algorithm was run using the optimization toolbox in MATLAB (R2021b, Mathworks). Several steps were taken to improve the likelihood of finding the global minimum, i.e. the best possible solution. First, the optimization will only stop once the average relative change in the cost function value is below $1e-6$ over 100 generations. Secondly, the cost function value for each iteration was visualized and inspected to check the optimization process for strange fluctuations. Lastly, the optimization was run five times to check for convergence to the same minimum.

4) *Selection of the final design*

In total, treadmill data of six subjects were used in this study. Of these six subjects, four were assigned to the selection group, and the remaining two were designated to the validation group. The selection group determined the optimal design, and the validation group validated this optimal design. Subjects were randomly distributed over both groups to ensure impartiality of the results, as shown in Table II.

Subject	Group	Height	Weight	Age	Gender
1	Selection	155 cm	51.0 kg	30 years	Female
4	Selection	173 cm	63.7 kg	26 years	Male
5	Selection	176 cm	63.6 kg	25 years	Male
6	Selection	171 cm	56.2 kg	23 years	Female
2	Validation	187 cm	72.5 kg	30 years	Male
3	Validation	181 cm	71.0 kg	30 years	Male

TABLE II: Distribution of the subjects over the selection group, used to determine the optimal design, and the validation group which validated the design. Demographic and anthropomorphic information of each subject is also included in this Table.

Design parameters and configurations were optimized for each of the four subjects in the selection group to determine their individual optimal setup. Consequently, each of these designs was evaluated on all four subjects in the selection group. The design with the best overall performance was selected, i.e. the design that would work best for general use. The chosen metric to evaluate the performance of each design is the mean of the cost function values of all four subjects in the selection group, i.e., the performance μ_j of design j with optimal configuration C_j and parameters $\vec{p}_j$ can be calculated as

$$\mu_j = \frac{\sum_{i=1}^{4} \psi_i(C_j, \vec{p}_j)}{4}. \tag{9}$$

The design with the lowest μ was selected as the final design and evaluated on the validation group.

D. *Validation of the optimal design*

The validation of the optimal design relies on the parasitic forces on the leg, as these should be minimal. The most critical factor here is that parasitic forces should not severely alter the gait. Therefore, a validation threshold should be set based on gait-altering forces. Ideally, the parasitic forces in MATE should not even cause discomfort. However, this first threshold gives a good indication of the magnitude of the parasitic forces. Moreover, if the gait alteration threshold is exceeded, it is clear that additional measures should be taken to decrease tendon length deviations during gait. The magnitude of the threshold should be dependent on the current stance of the subject, i.e. the threshold should be variable over the gait cycle. Specific stances could be more susceptible to perturbations, so such a variable threshold is important to evaluate the final design accurately.

Severini et al. found that perturbations of $A_\mathrm{x} = 0.092\,(\mathrm{N}\cdot\mathrm{s})/(\mathrm{Kg}{\cdot}\mathrm{m})$ in the x-direction and $A_\mathrm{z} = -0.058\,(\mathrm{N}\cdot\mathrm{s})/(\mathrm{Kg}{\cdot}\mathrm{m})$ in the z-direction induced an increase in step length of about $30\,\%$ [32]. These values were used to create the mass normalized force thresholds $\vec{T}_{\mathrm{x},j}$ and $\vec{T}_{\mathrm{z},j}$ over the entire gait trajectory in the x- and z-direction, which the parasitic forces were evaluated against. This was achieved by multiplying with the respective velocity $\mathbf{v}_\mathrm{x}$ and $\mathbf{v}_\mathrm{z}$ over the entire gait trajectory, as shown in Equation 10 and 11:

$$\vec{T}_{\mathrm{x},j} = A_\mathrm{x}\vec{v_\mathrm{x}}, \tag{10}$$

$$\vec{T}_{\mathrm{z},j} = A_\mathrm{z}\vec{v_\mathrm{z}}. \tag{11}$$

The absolute value of the mass normalized forces $\hat{\vec{F}}_j$ should be below the set threshold $\vec{T}_j$ at all times, where $\vec{T}_j = [\vec{T}_{\mathrm{x},j} \quad \vec{T}_{\mathrm{z},j}]$. Hence, to validate that the parasitic forces in MATE do not alter the gait pattern, the following equation should be met at all times t, i.e.

$$|\hat{\vec{F}}_j(t)| \leq |\vec{T}_j(t)|\ \forall\, t. \tag{12}$$

This equation was evaluated in both the left and right leg to validate the optimal design.

III. RESULTS

A. Possible configurations for MATE

because MATE has similar working principles at the front and back, only the possible configurations for the front are examined. Four pulleys are selected for the design, i.e. $n_\mathrm{p} = 4$ as shown in Figure 4. Four pulleys allow full control of the x-, y-, and z-position of each leg within the workspace by having tendons in all of these directions.

The amount of pulley configurations $n_\mathrm{p,c}$ is also constrained by the requirement for control of all translational DoF. Translational control in the x-direction is realized by having tendons in both the positive and negative x-direction, i.e. the front and back of the subject. Furthermore, tendons should point in both the positive and negative y- and z-direction relative to the leg for each leg. Accordingly, one set of pulleys must be narrow, and one set should be wide, and one set should be above the attachment point and one set below it. This only leaves 2 possible pulley configurations, i.e. $n_\mathrm{p,c} = 2$. The first pulley configuration can be seen in the two left images of Figure 4, and the second pulley configuration is shown in the two right images.

Each tendon is connected via two of the four pulleys, because this is required for full control of all DoF. Only connecting a tendon to one pulley reduces manipulability. Furthermore, connecting a tendon to 3 or more pulleys limits the available pulleys for the other tendon. Therefore, $n_\mathrm{p,t} = 2$. Now Equation 1 can be solved,

$$n_\mathrm{conftoot} = \frac{4!}{2} \cdot 2 = 24. \tag{13}$$

All 24 potential configurations are designed and evaluated and can be found in Appendix A. Due to the two tendons being identical, only 12 possible designs remain, as it does not matter if the tendons are switched. A further motion analysis reveals that 8 of the remaining configurations reduce control or cause tendon collisions, leaving $n_\mathrm{conf} = 4$ valid configurations, which are shown in Figure 4.

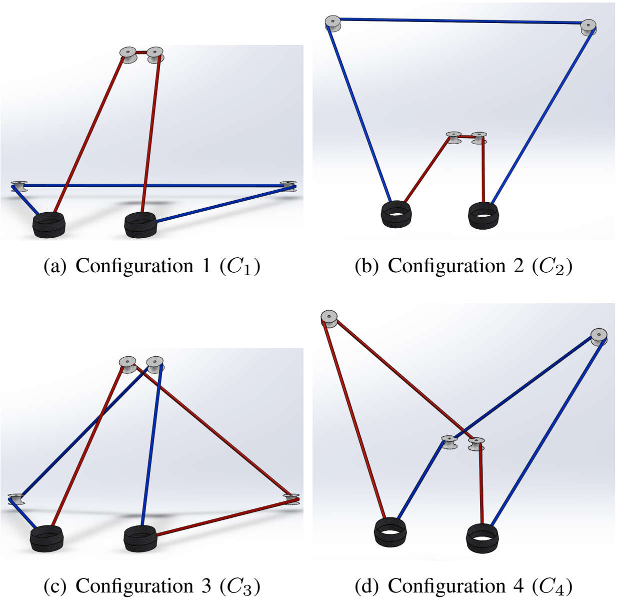
(a) Configuration 1 (C_1)
(b) Configuration 2 (C_2)
(c) Configuration 3 (C_3)
(d) Configuration 4 (C_4)

Fig. 4: All valid configurations that can be used for MATE. Only the front side of the robot is depicted, as an identical working principle is used at the front and the back of the subject. These configurations are used as input for the optimization.

B. Obtaining and pre-processing of gait data

The low-pass filtered left hip marker data (L_FMH) of subject one is shown in Figure 5. Undesired movement in the sagittal (x) and transversal (y) direction over time can be seen here. Subtracting this filtered data from all marker data removes this drift, which is done for all subjects. Only the results of subject one are shown, as the results are very similar for all subjects. Raw, filtered, and processed marker data of all subjects are present in Appendix B.

C. Finding the optimal design

The optimization results for each subject in the selection group are shown in Table III. Each of the subjects achieves the

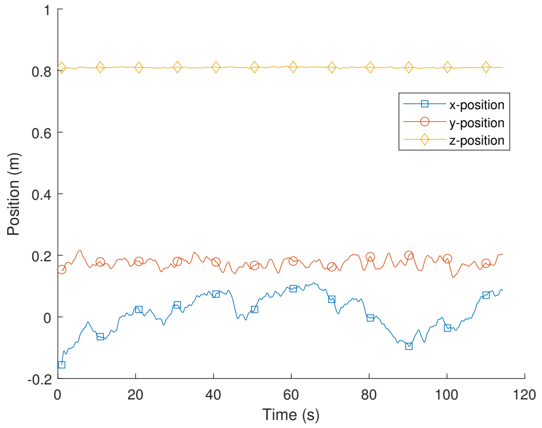

Fig. 5: Low-pass filtered hip marker (L_FMH) data of subject one with a cutoff frequency of $0.5\,\mathrm{Hz}$ using a minimal order filter. Here the drift in both the x- and y-direction can be seen.

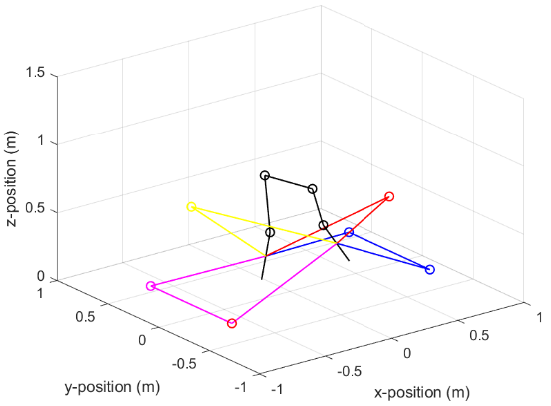

Fig. 6: Optimal design of MATE determined on participants of the selection group. This design was optimized on subject one, and had the lowest mean cost function μ of all members of the selection group.

best results, i.e. lowest cost function value, when configuration one is used both at the front and back. The optimal parameters z_2, w_4, and z_4 are identical for each subject, while w_1, z_1, w_2, w_3, and z_3 show some inter-subject variations. Overall the optimal designs are all relatively similar, especially since the same configuration is optimal for each subject.

Evaluation results of the optimal design of each subject are shown in Table IV. Here for each design, the cost function value ψ_i is calculated based on the gait data of subject i. The mean of the cost function values of each design μ is also shown. Overall the gait data of subject five resulted in the highest cost function values for all designs. Furthermore, the optimal design of subject five produced the highest cost function values over all subjects, demonstrated by the highest μ value of $33.0\,\mathrm{N}$. The optimal design of Subject one produced the lowest mean cost function value μ of $32.1\,\mathrm{N}$, and is thus selected as the best general design. This design is used for validation on the validation group and is shown in Figure 6. Orthographic views of the optimal designs for all four subjects are shown in Appendix C.

D. Validation of the optimal design

The validation on subject two with the optimal design did not satisfy Equation 12. The resulting forces $|\hat{F}_2|$ in combination with the thresholds $|T_2|$ are visualized in Figure 7. Here only one gait cycle of the left leg is displayed for clarity of the results. This specific gait cycle contains the maximum mass normalized absolute force in the x-direction of $|\hat{F}_{2,\mathrm{x}}| = 0.421\,\mathrm{N/kg}$. The maximum value in the z-direction is $|\hat{F}_{2,\mathrm{z}}| = 0.0683\,\mathrm{N/kg}$. In contrast, the threshold values at these points are $|T_{2,x}| = 0.0413\,\mathrm{N/kg}$ and $|T_{2,z}| = 5.33 \times 10^{-4}\,\mathrm{N/kg}$, and are thus clearly exceeded. The validation results of subject 3 are shown in Figure 8, where again one step containing the highest $|\hat{F}_{2,\mathrm{x}}|$ is visualized, which was also in the left leg. Here again the threshold $|T_2|$ is clearly exceeded. This is also shown by results of the peak forces and their respective thresholds, which are $|\hat{F}_{2,\mathrm{x}}| = 0.394\,\mathrm{N/kg}$ and $|\hat{F}_{2,\mathrm{z}}| = 0.0627\,\mathrm{N/kg}$, which have thresholds of $|T_{2,x}| = 0.0476\,\mathrm{N/kg}$ and $|T_{2,z}| = 0.0134\,\mathrm{N/kg}$. All 10 gait cycles of both subjects are visualized in Appendix D.

Further inspection of the visualizations in Figures 7 and 8 reveal that the peaks of the forces do not align with the peaks of the threshold. Peak forces appear four times each gait cycle, during loading response, terminal stance, pre-swing and terminal swing. Peak threshold values are achieved when velocities are maximal, which appear twice each gait cycle around mid-stance and mid-swing.

IV. DISCUSSION

This research aimed to determine whether subjects' legs could be directly connected with tendons without producing parasitic forces that lie above a gait-altering threshold. We conducted thorough research on all possible configurations and parameters for a system with four tendons and 3 DoF per leg to achieve this. After this, we performed a double optimization on both the configuration and parameters, resulting in an optimal design for MATE. This optimal design was evaluated to analyze the magnitude of the parasitic forces.

Subject	C_{front}	C_{rear}	w_1	z_1	w_2	z_2	w_3	z_3	w_4	z_4
1	C_1	C_1	0.00 m	0.50 m	0.40 m	0.10 m	0.00 m	0.82 m	0.40 m	0.10 m
4	C_1	C_1	0.00 m	0.50 m	0.20 m	0.10 m	0.00 m	0.81 m	0.40 m	0.10 m
6	C_1	C_1	0.05 m	0.50 m	0.40 m	0.10 m	0.05 m	1.00 m	0.40 m	0.10 m
5	C_1	C_1	0.00 m	0.63 m	0.40 m	0.10 m	0.05 m	0.73 m	0.40 m	0.10 m

TABLE III: Optimal design solution for each subject in the selection group. The optimal configuration for the front C_{front} and rear C_{rear} are shown in combination with the best possible parameters.

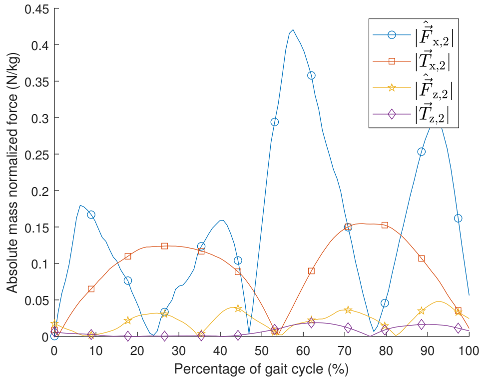

Fig. 7: Validation results of the optimal design on subject 2. One gait cycle of the left leg is selected for clarity of the visualization. The normalized force $|\hat{F}_2|$ clearly exceeds the threshold $|T_2|$ in both the x- and z-direction.

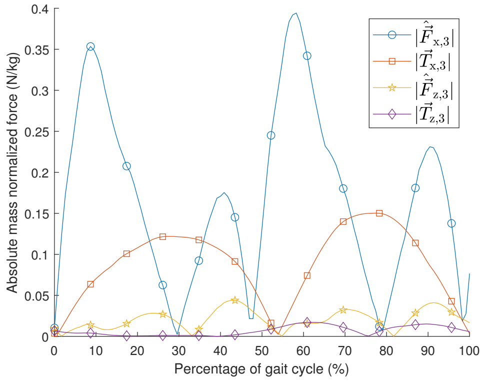

Fig. 8: Validation results of the optimal design on subject 3. One gait cycle of the left leg is selected for clarity of the visualization. The normalized force $|\hat{F}_2|$ clearly exceeds the threshold $|T_2|$ in both the x- and z-direction.

Optimal design	ψ_4	ψ_1	ψ_6	ψ_5	μ
1	30.8 N	28.3 N	34.3 N	34.9 N	32.1 N
4	30.5 N	29.1 N	35.9 N	36.2 N	32.9 N
6	30.7 N	28.6 N	34.2 N	35.1 N	32.2 N
5	32.0 N	29.7 N	35.7 N	34.9 N	33.0 N

TABLE IV: Cost function value $C_{\mathrm{fun},i}$ based on the gait data of subject i, calculated for the optimal design of each subject.

The optimization algorithm selected configuration one, which has horizontal tendons and narrow pulleys at the top for both the front and back for all subjects. This strongly indicates that configuration one produces the least parasitic forces. The width parameters w_1, w_2, w_3 and w_4 mostly appear to push towards the lower bound for the narrow top tendons and the upper bound for the wider bottom tendons. These findings could suggest the tendons want to be as orthogonal to the gait trajectory as possible, as this might result in minimum tendon elongation $\vec{u_{\mathrm{t}}}$, and thus minimal forces according to Equation 3. The height parameters z_1, z_2 and z_4 pushing towards the lower bound align with this assumption; however, z_3 does not follow this trend. The optimal designs for each subject are relatively similar, with the final optimal design of subject one only slightly outperforming the others. Subject one is the lightest and shortest out of all the subjects, which might be why she scored the lowest on all designs. This might also affect the outcome metric μ, and warrants the need for mass normalization in the cost function for future research.

Validation of the design indicates that potential gait-altering forces are produced on both subjects in the validation group. Possibly a lower stiffness could still be effectively implemented. However, gait phases where parasitic forces occur seem extra susceptible to perturbations based on the variable mass normalized force thresholds. Therefore, the best solution for further research appears to be implementing a compensation method for the tendon length deviation. One possible solution is implementing a variable radius winch for each tendon, as done in the RYSEN [18]. Another possibility is using non-circular pulleys, which can change their radius to adjust tendon length [33]. Lastly, the pulleys could potentially be linearly actuated to compensate for tendon length deviations. However, this would defeat the purpose of creating a minimally actuated device.

A limitation of this study is that it relies solely on simulations. As shown by similar research, which simulated and optimized a passive exoskeleton for gait [34], actual subject studies with the optimized design can yield vastly different results [35]. Human interaction is difficult to model, and with simulations of motion capture data, the assumption is made that the subject does not adjust to MATE. This warrants a study with human subjects and MATE to check whether the parasitic forces are as problematic as calculated here.

Another limitation is that the data was collected during free treadmill walking, which likely differs from actual movement in MATE. This difference is partially compensated by preparing and filtering the data; however, this further highlights the need for subject tests with MATE.

Therefore, future research recommendations mainly start with a subject study using MATE, where motion capture is used and forces are monitored. Questionnaires could be used to indicate discomfort. Based on these preliminary results, it could be determined whether tendon length deviation compensation is required. When this has been addressed, a clinical trial with stroke patients should be conducted to test if significant gait improvements can be achieved by MATE, compared to a control group receiving conventional gait rehabilitation. Clinical testing with stroke patients might reveal additional limitations, as the design has been optimized for healthy subjects.

For now, these results present the first stepping stone towards a simplistic yet possibly effective rehabilitation device. The current state-of-the-art in rehabilitation robotics continually becomes more advanced and sophisticated. However, this increasing complexity can limit their actual usability and affordability. A minimally actuated device like MATE could be a more approachable solution due to its simplicity in use and affordability. Moreover, this could increase the availability in poorer regions, where people also need stroke rehabilitation, and funds might be limited.

V. CONCLUSION

This research consists of a simulated optimization and validation of a preliminary design of MATE, a Minimally Actuated Tendon-based Exercise environment. The aim was to check whether a subject's legs can be connected directly with tendons without producing gait altering parasitic forces. A comparison of the parasitic forces produced by MATE during healthy gait with known gait altering forces indicates that this seems to not be possible at the moment. A compensation method is required to compensate for tendon length variations to reduce these parasitic forces. However, this research takes an important first step towards designing a simplistic yet possibly effective gait rehabilitation robot.

REFERENCES

[1] WHO. (2019) Global health estimates. [Online]. Available: https://www.who.int/data/stories/leading-causes-of-death-and-disability-2000-2019-a-visual-summary

[2] M. P. Lindsay, B. Norrving, R. L. Sacco, M. Brainin, W. Hacke, S. Martins, J. Pandian, and V. Feigin, "World stroke organization (wso): global stroke fact sheet 2019," 2019.

[3] H. S. Jørgensen, H. Nakayama, H. O. Raaschou, and T. S. Olsen, "Recovery of walking function in stroke patients: the copenhagen stroke study," *Archives of physical medicine and rehabilitation*, vol. 76, no. 1, pp. 27–32, 1995.

[4] P. Langhorne, J. Bernhardt, and G. Kwakkel, "Stroke rehabilitation," *The Lancet*, vol. 377, no. 9778, pp. 1693–1702, 2011.

[5] R. P. Van Peppen, G. Kwakkel, S. Wood-Dauphinee, H. J. Hendriks, P. J. Van der Wees, and J. Dekker, "The impact of physical therapy on functional outcomes after stroke: what's the evidence?" *Clinical rehabilitation*, vol. 18, no. 8, pp. 833–862, 2004.

[6] D. R. Louie and J. J. Eng, "Powered robotic exoskeletons in post-stroke rehabilitation of gait: a scoping review," *Journal of neuroengineering and rehabilitation*, vol. 13, no. 1, p. 53, 2016.

[7] R. Dickstein, "Rehabilitation of gait speed after stroke: a critical review of intervention approaches," *Neurorehabilitation and neural repair*, vol. 22, no. 6, pp. 649–660, 2008.

[8] A. Pennycott, D. Wyss, H. Vallery, V. Klamroth-Marganska, and R. Riener, "Towards more effective robotic gait training for stroke rehabilitation: a review," *Journal of neuroengineering and rehabilitation*, vol. 9, no. 1, pp. 1–13, 2012.

[9] J.-M. Belda-Lois, S. Mena-del Horno, I. Bermejo-Bosch, J. C. Moreno, J. L. Pons, D. Farina, M. Iosa, M. Molinari, F. Tamburella, A. Ramos *et al.*, "Rehabilitation of gait after stroke: a review towards a top-down approach," *Journal of neuroengineering and rehabilitation*, vol. 8, no. 1, p. 66, 2011.

[10] S. Hesse, A. Waldner, and C. Tomelleri, "Innovative gait robot for the repetitive practice of floor walking and stair climbing up and down in stroke patients," *Journal of neuroengineering and rehabilitation*, vol. 7, no. 1, p. 30, 2010.

[11] J. Mehrholz, S. Thomas, C. Werner, J. Kugler, M. Pohl, and B. Elsner, "Electromechanical-assisted training for walking after stroke," *Cochrane Database of Systematic Reviews*, no. 5, 2017.

[12] D. J. Reinkensmeyer, D. Aoyagi, J. L. Emken, J. A. Galvez, W. Ichinose, G. Kerdanyan, S. Maneekobkunwong, K. Minakata, J. A. Nessler, R. Weber *et al.*, "Tools for understanding and optimizing robotic gait training." *Journal of rehabilitation research and development*, vol. 43, no. 5, pp. 657–670, 2006.

[13] L. Marchal-Crespo and R. Riener, "Robot-assisted gait training," in *Rehabilitation Robotics*. Elsevier, 2018, pp. 227–240.

[14] M. F. Bruni, C. Melegari, M. C. De Cola, A. Bramanti, P. Bramanti, and R. S. Calabrò, "What does best evidence tell us about robotic gait rehabilitation in stroke patients: a systematic review and meta-analysis," *Journal of Clinical Neuroscience*, vol. 48, pp. 11–17, 2018.

[15] A. Duschau-Wicke, J. Von Zitzewitz, A. Caprez, L. Lunenburger, and R. Riener, "Path control: a method for patient-cooperative robot-aided gait rehabilitation," *IEEE Transactions on Neural Systems and Rehabilitation Engineering*, vol. 18, no. 1, pp. 38–48, 2009.

[16] H. Vallery, M. Guidali, A. Duschau-Wicke, and R. Riener, "Patient-cooperative control: providing safe support without restricting movement," in *World Congress on Medical Physics and Biomedical Engineering, September 7-12, 2009, Munich, Germany*. Springer, 2009, pp. 166–169.

[17] G. Carpino, A. Pezzola, M. Urbano, and E. Guglielmelli, "Assessing effectiveness and costs in robot-mediated lower limbs rehabilitation: a meta-analysis and state of the art," *Journal of healthcare engineering*, vol. 2018, 2018.

[18] M. Plooij, U. Keller, B. Sterke, S. Komi, H. Vallery, and J. Von Zitzewitz, "Design of rysen: an intrinsically safe and low-power three-dimensional overground body weight support," *IEEE Robotics and Automation Letters*, vol. 3, no. 3, pp. 2253–2260, 2018.

[19] X. Jin, A. Prado, and S. K. Agrawal, "Retraining of human gait-are lightweight cable-driven leg exoskeleton designs effective?" *IEEE Transactions on Neural Systems and Rehabilitation Engineering*, vol. 26, no. 4, pp. 847–855, 2018.

[20] Y. Zou, N. Wang, X. Wang, H. Ma, and K. Liu, "Design and experimental research of movable cable-driven lower limb rehabilitation robot," *IEEE Access*, vol. 7, pp. 2315–2326, 2018.

[21] R. Hidayah, X. Jin, S. Chamarthy, M. M. Fitzgerald, and S. K. Agrawal, "Comparing the performance of a cable-driven active leg exoskeleton (c-alex) over-ground and on a treadmill," in *2018 7th IEEE International Conference on Biomedical Robotics and Biomechatronics (Biorob)*. IEEE, 2018, pp. 299–304.

[22] R. Hidayah, S. Chamarthy, A. Shah, M. Fitzgerald-Maguire, and S. K. Agrawal, "Walking with augmented reality: A preliminary assessment of visual feedback with a cable-driven active leg exoskeleton (c-alex)," *IEEE Robotics and Automation Letters*, vol. 4, no. 4, pp. 3948–3954, 2019.

[23] R. Hidayah, L. Bishop, X. Jin, S. Chamarthy, J. Stein, and S. K. Agrawal, "Gait adaptation using a cable-driven active leg exoskeleton (c-alex) with post-stroke participants," *IEEE Transactions on Neural Systems and Rehabilitation Engineering*, vol. 28, no. 9, pp. 1984–1993, 2020.

[24] S. C. Cramer, M. Sur, B. H. Dobkin, C. O'brien, T. D. Sanger, J. Q. Trojanowski, J. M. Rumsey, R. Hicks, J. Cameron, D. Chen *et al.*, "Harnessing neuroplasticity for clinical applications," *Brain*, vol. 134, no. 6, pp. 1591–1609, 2011.

[25] S. J. Olney and C. Richards, "Hemiparetic gait following stroke. part i: Characteristics," *Gait & posture*, vol. 4, no. 2, pp. 136–148, 1996.

[26] S. Fang, *Design, modeling and motion control of tendon based parallel manipulators*. VDI-Verlag, 2005.

[27] J. L. Emken, S. J. Harkema, J. A. Beres-Jones, C. K. Ferreira, and D. J. Reinkensmeyer, "Feasibility of manual teach-and-replay and continuous impedance shaping for robotic locomotor training following spinal cord injury," *IEEE Transactions on Biomedical Engineering*, vol. 55, no. 1, pp. 322–334, 2007.

[28] S. Maggioni, N. Reinert, L. Lünenburger, and A. Melendez-Calderon, "An adaptive and hybrid end-point/joint impedance controller for lower limb exoskeletons," *Frontiers in Robotics and AI*, vol. 5, p. 104, 2018.

[29] H. Vallery, J. Veneman, E. Van Asseldonk, R. Ekkelenkamp, M. Buss, and H. Van Der Kooij, "Compliant actuation of rehabilitation robots," *IEEE Robotics & Automation Magazine*, vol. 15, no. 3, pp. 60–69, 2008.

[30] T. van den Boom and B. de Schutter, "Optimiztion in systems and control," 2018. [Online]. Available: https://www.webedu.nl/bestellen/tudelft/

[31] D. E. Goldberg and J. H. Holland, "Genetic algorithms and machine learning," 1988.

[32] G. Severini, A. Koenig, C. Adans-Dester, I. Cajigas, V. C. Cheung, and P. Bonato, "Robot-driven locomotor perturbations reveal synergy-mediated, context-dependent feedforward and feedback mechanisms of adaptation," *Scientific reports*, vol. 10, no. 1, pp. 1–16, 2020.

[33] D. Fedorov and L. Birglen, "Differential noncircular pulleys for cable robots and static balancing," *Journal of Mechanisms and Robotics*, vol. 10, no. 6, p. 061001, 2018.

[34] A. J. Van den Bogert, "Exotendons for assistance of human locomotion," *Biomedical engineering online*, vol. 2, no. 1, pp. 1–8, 2003.

[35] W. van Dijk and H. Van der Kooij, "Xped2: A passive exoskeleton with artificial tendons," *IEEE robotics & automation magazine*, vol. 21, no. 4, pp. 56–61, 2014.

[36] A. Cappozzo, F. Catani, U. Della Croce, and A. Leardini, "Position and orientation in space of bones during movement: anatomical frame definition and determination," *Clinical biomechanics*, vol. 10, no. 4, pp. 171–178, 1995.

APPENDIX

A: Possible configurations for MATE

All possible configurations have to be considered to obtain the best result from the optimization. Therefore, a systematic approach was implemented to find all these possible solutions. At least four tendons are required to actuate the x-, y-, and z-position of a leg. Control in the x-plane, or sagittal plane, is realized with tendons at the front and back of the subject. For full control in the y-plane, or transversal plane, tendons should point both inwards and outwards, i.e. in the negative and positive y-direction relative to the leg. This is realized by having two narrow and two wide sets of pulleys. For control in the z-plane, or up and downwards direction, two sets of pulleys are placed above the endpoint trajectory, and two sets of pulleys are placed below it. These requirements result in two possible pulley configurations $n_{\mathrm{p,c}}$, which are shown in Figure 9.

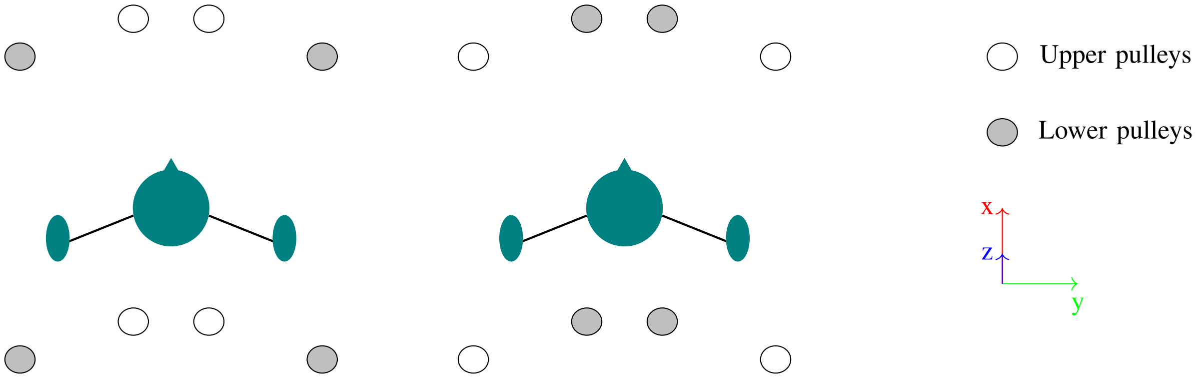

Fig. 9: Top view of both possible pulley configurations that allow for full control of the x-, y-, and z-position of the legs.

Tendon configurations follow the same principles on the front and back of the subject, so only the front will be considered to determine possible configurations. These configurations are then evaluated at the front and back of the subject separately to fully check all possible configurations. With the number of pulleys to connect to $n_{\mathrm{p}} = 4$, The amount of pulley configurations $n_{\mathrm{p,c}} = 2$ as shown in Figure 9, and 2 tendons per pulley $n_{\mathrm{p,t}} = 2$, Equation 1 can be computed:

$$n_{\mathrm{c,t}} = \frac{4!}{2} \cdot 2 = 24. \tag{14}$$

As previously mentioned, the tendons are identical and can thus be swapped, leaving 12 unique configurations. All these configurations are constructed and shown in Figures 10 and 11. Here, Figure 10 contains the pulley configuration where the top 2 pulleys are narrow, while Figure 11 shows the pulley configuration where the top 2 pulleys are wide. It can clearly be seen in both Figures that the bottom row does not allow for full control of the y-position, as the tendons are all pointing inwards. Furthermore, a motion analysis using simulations of gait reveals that all these configurations suffer from tendon collisions. Tendon collisions severely hinder usability, and these configurations are therefore not considered. Moreover, the previously mentioned motion analysis also reveals that the rightmost design in the top row of both Figures suffers from tendon collisions during gait. Therefore, only the first two designs of both Figures are feasible for actual use. Therefore, these four configurations are chosen as Configuration 1, 2, 3, and 4 and used as input for the optimization. A more realistic render of the feasible configurations can be seen in Figure 4.

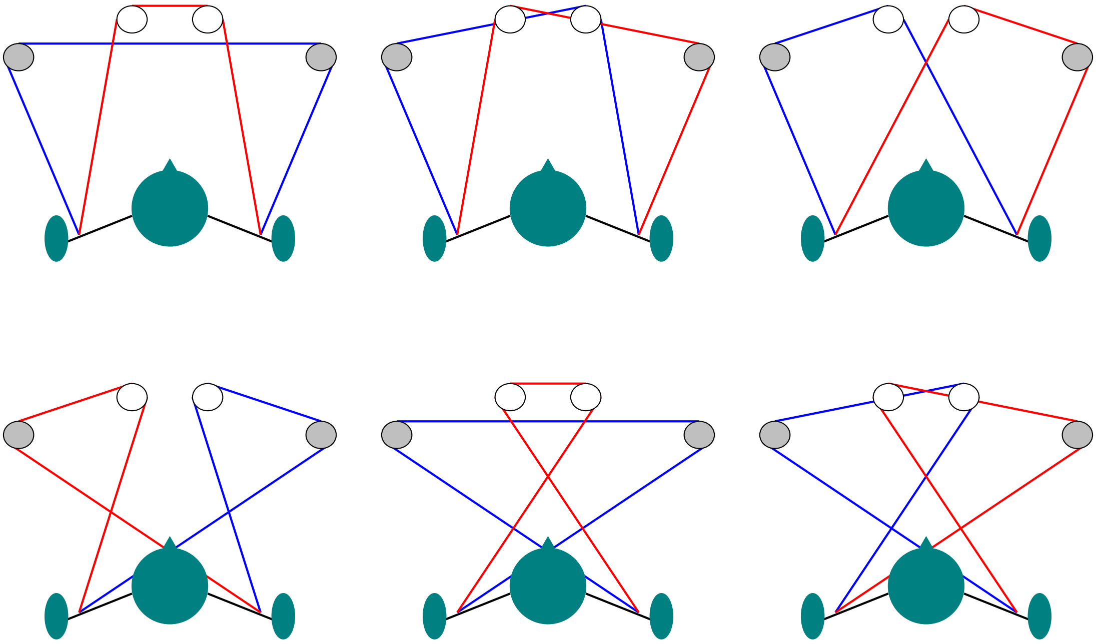

Fig. 10: Top view of all possible tendon configurations at the front of the subjects when the top pulleys are narrow and the bottom pulleys are wide.

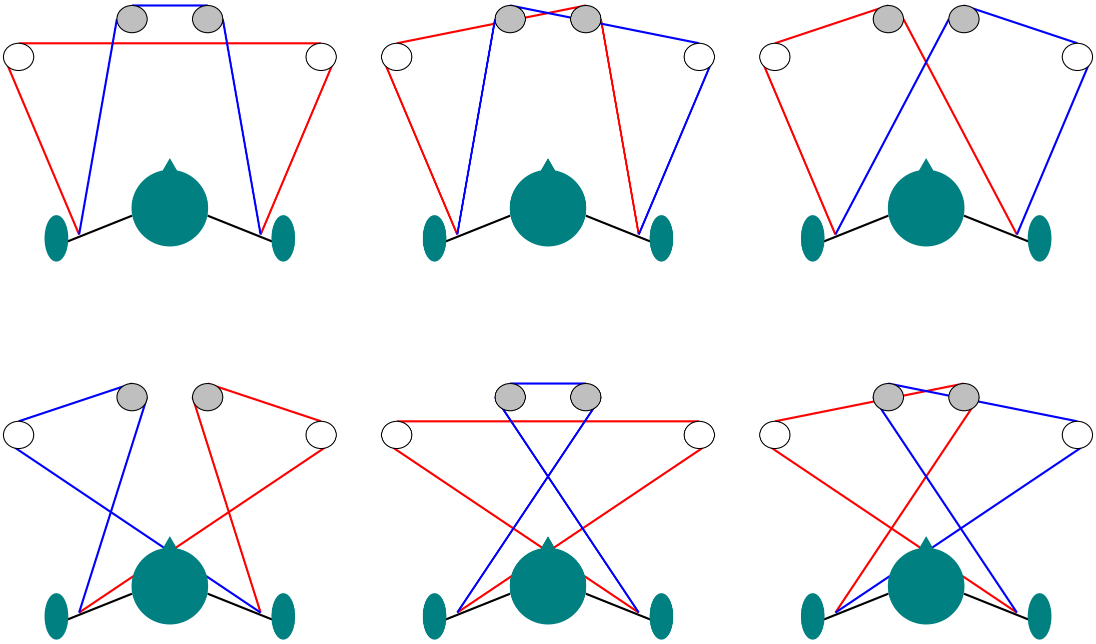

Fig. 11: Top view of all possible tendon configurations at the front of the subjects when the top pulleys are wide and the bottom pulleys are narrow.

B: Obtaining and pre-processing of gait data

The subject data used in this thesis was obtained by Saher Jabeen for a yet to be published study. It contains motion capture data with markers of healthy subjects freely walking on a treadmill. The data is recorded at a sampling frequency of $f_\mathrm{s} = 100\,\mathrm{Hz}$. Seven Subjects are recorded; however, some marker data of subject seven was missing, so subject seven is excluded from this thesis. The marker data of the remaining six subjects is used to create a gait simulation of each subject.

Relevant markers have been selected and processed to reconstruct the legs. The GT marker represents the hip joint, as shown in Figure 12(a). The knee joint is represented by the average of LE and ME to represent best the middle of the joint, which can be seen in Figure 12(b). Similarly, the ankle is defined by the average of LM and MM, as depicted in Figure 12(c). Heelstrikes are identified with the marker closest to the heel, CA, which is also shown in Figure 12(c). The implemented variable names for each selected landmark is shown in Table V.

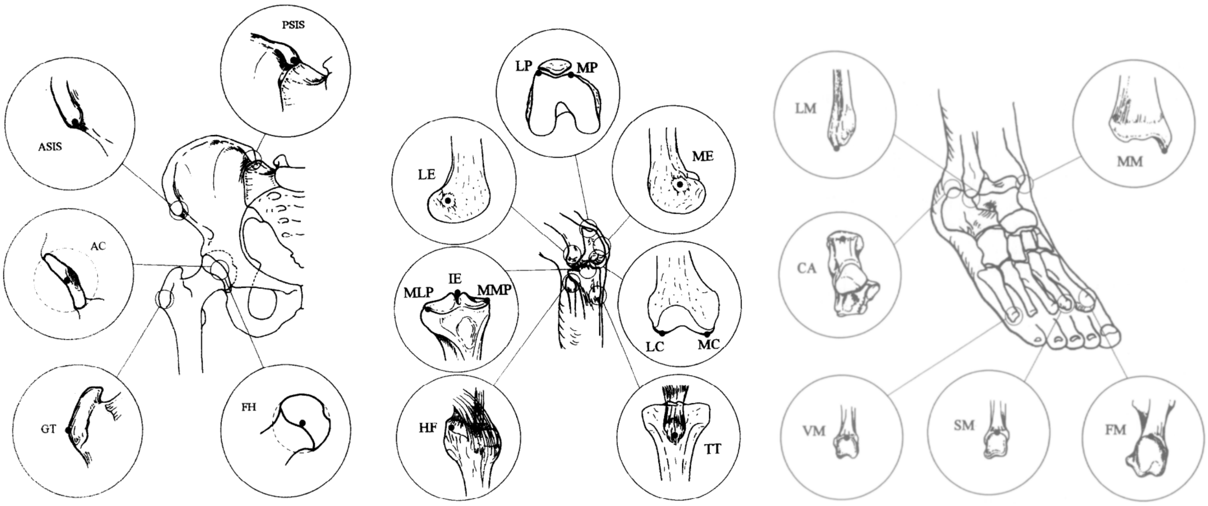

(a) Anatomical markers on the hip joint (b) Anatomical markers on the knee joint (c) Anatomical markers on the ankle joint

Fig. 12: Anatomical landmark points used for marker placement in motion capture. Image obtained from Cappozzo et al [36]

.

Anatomical landmark	GT	LE	ME	LM	MM	CA
Left leg variable	L_FMH	L_FLE	L_FME	L_LM	L_MM	L_CAL
Right leg variable	R_FMH	R_FLE	R_FME	R_LM	R_MM	R_CAL

TABLE V: Variable names used in the simulation in MATLAB for each of the anatomical landmarks.

A static capture of the subjects is used to create a local frame. Subtracting this local frame from each data point moves the simulation to the origin. After this, the data is rotated with -90° around the z-axis to align the sagittal plane with the x-axis. The simulation can be seen in Figure 13, where one full gait cycle is performed over each of the subjects. The motion capture resulted in some missing data points, which are filled with the Matlab function “fillgaps”. This function uses autoregressive modelling to estimate missing values in a dataset.

The first 50 seconds of each dataset are disregarded, as this time is needed to speed up and reach a steady gait. The total remaining data span is around 80 seconds for each subject. Ten full gait cycles of each subject are used in the optimization and validation, as this better represents the variability of gait. These gait cycles are chosen at random from the remaining 80 seconds of gait data. They are identified by monitoring the heel marker CA, whose minimal value indicates a heel strike. The total dataset of CA of subject two is shown in Figure 14.

MATE will presumably centre subjects on the treadmill, as deviations will be met with a correcting force. Data was recorded during free walking on a treadmill, which results in deviations in both the transversal and sagittal direction. These deviations can be seen in the unfiltered left hip positions in Figure 15. Therefore, a low-pass filter is applied on the left hip marker, L_FMH of each subject, and subtracted from the entire data set. The chosen low-pass filter is a minimum-order filter and has a stopband attenuation of $60\,\mathrm{dB}$. The filter is applied in both directions to prevent phase shift. A cutoff frequency of $\omega_\mathrm{c} = 0.5\,\mathrm{Hz}$ is implemented, which has iteratively been determined to maintain step variability but remove sagittal and transversal variability. The filtered hip signal for each subject is shown in Figure 16. Subtracting a low-pass filter of the hip marker of each signal will shift the hip marker to $x, y, z = (0\,\mathrm{m}, 0\,\mathrm{m}, 0\,\mathrm{m})$. Therefore, the static L_FMH position is subsequently added to each marker to compensate for this shift. However, the x-position will not be compensated, as the subject should be centred here. Sensor noise filtering is not required, as this will not influence the optimization and thus could only reduce the reliability of the result. The final centred marker data of the left hip is displayed in Figure 17.

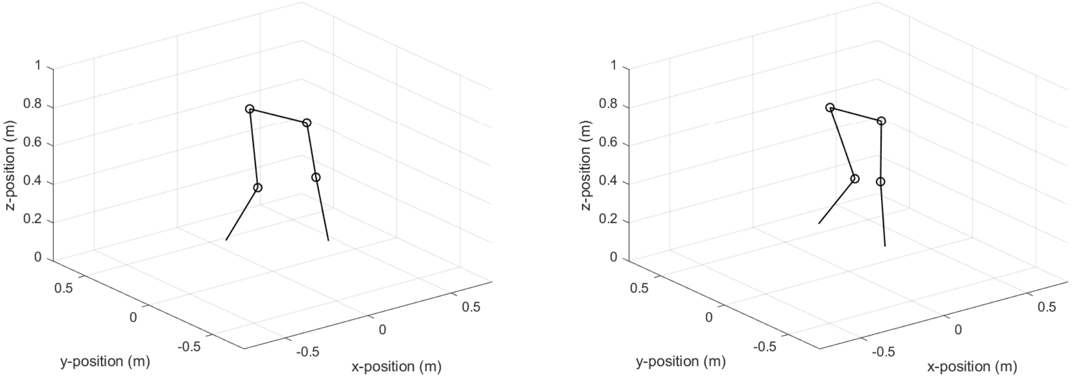

(a) Subject 1

(b) Subject 2

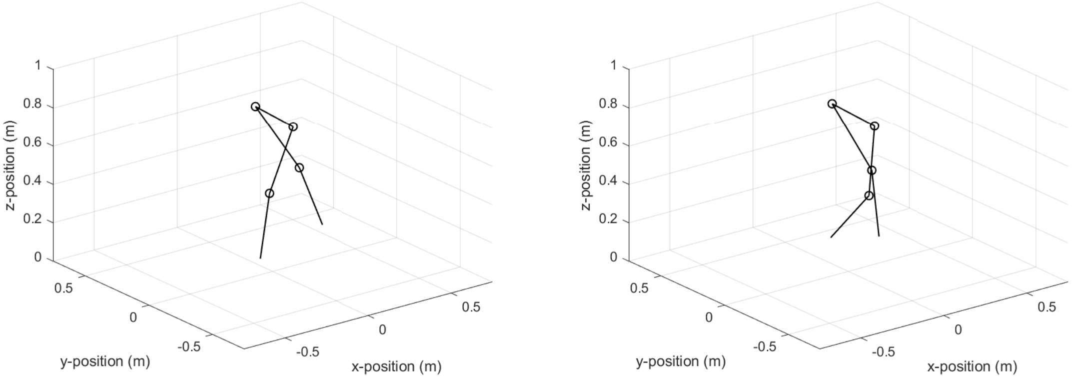

(c) Subject 3

(d) Subject 4

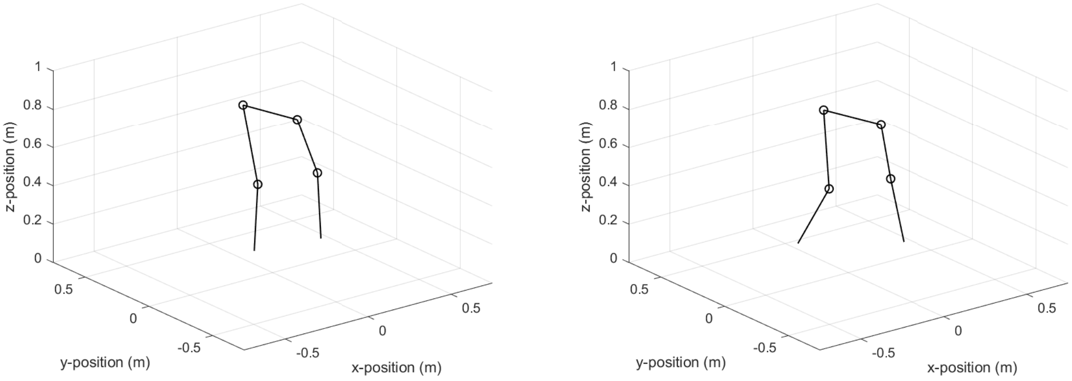

(e) Subject 5

(f) Subject 6

Fig. 13: Reconstruction of the gait in a simulation from marker data for each of the 6 subjects. Over all the subjects one full gait cycle of the simulation can be seen.

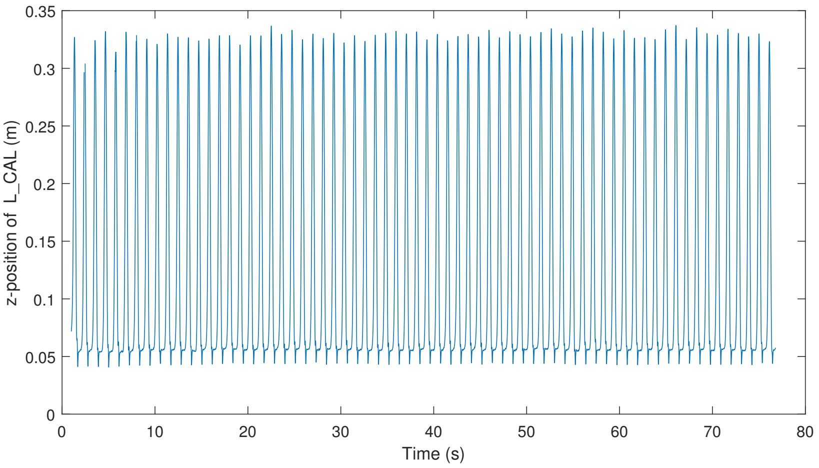

Fig. 14: CA Marker of subject 2 over time. This image contains the total steady gait dataset available, from which 10 gait cycles are selected at random. Some intra step variability can be observed in the step height z, which is desired for a realistic optimization and validation.

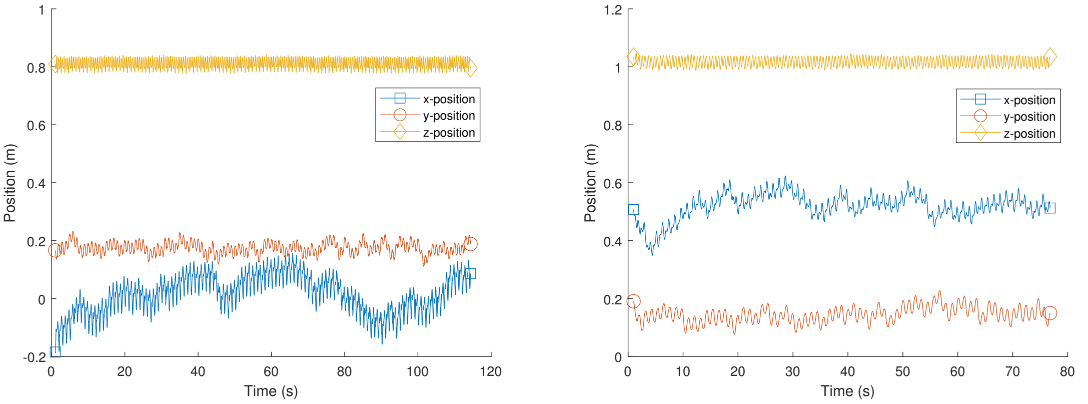

(a) Subject 1 (b) Subject 2

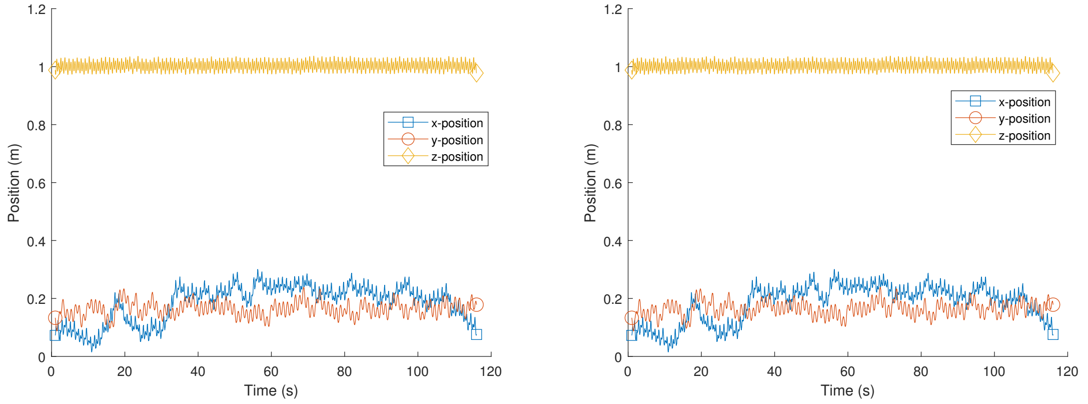

(c) Subject 3 (d) Subject 4

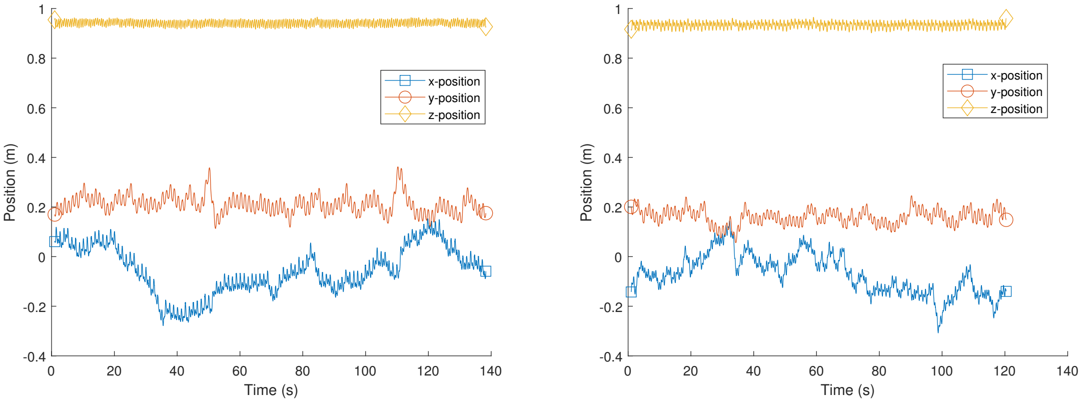

(e) Subject 5 (f) Subject 6

Fig. 15: Unfiltered position of the left hip marker, L_FMH, for each of the subjects. Clearly movement variation in both the saggital and transversal direction can be observed.

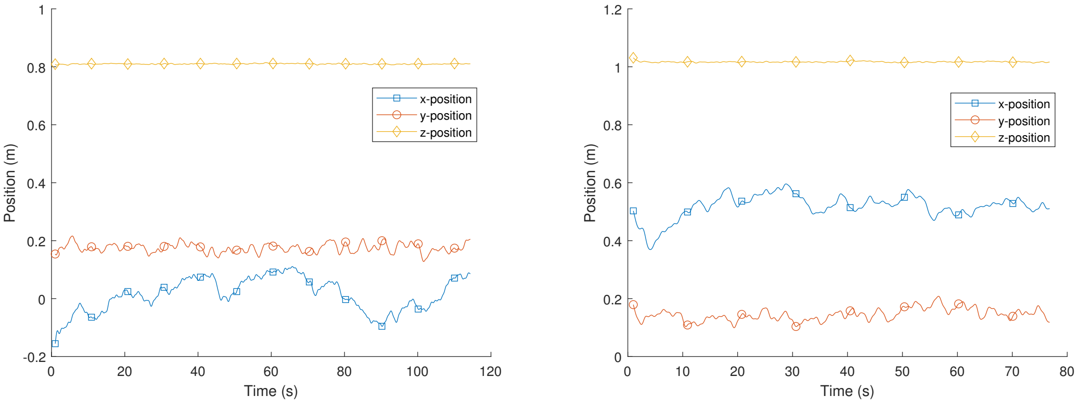

(a) Subject 1 (b) Subject 2

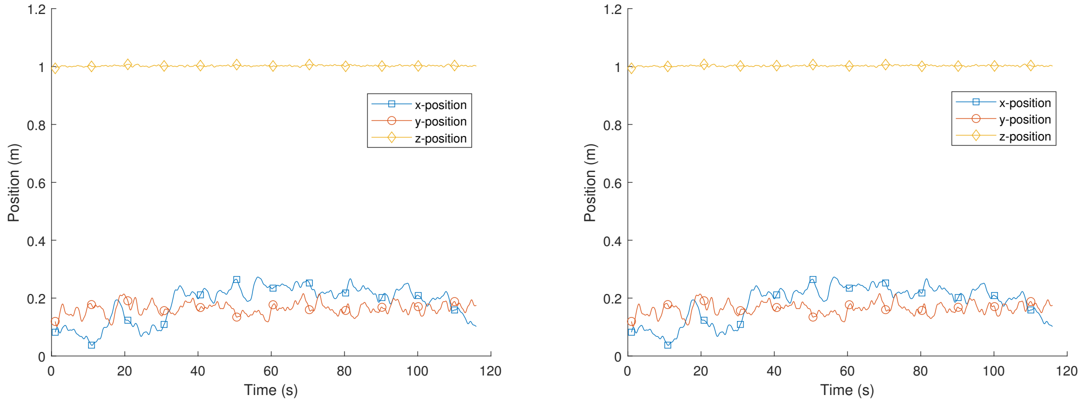

(c) Subject 3 (d) Subject 4

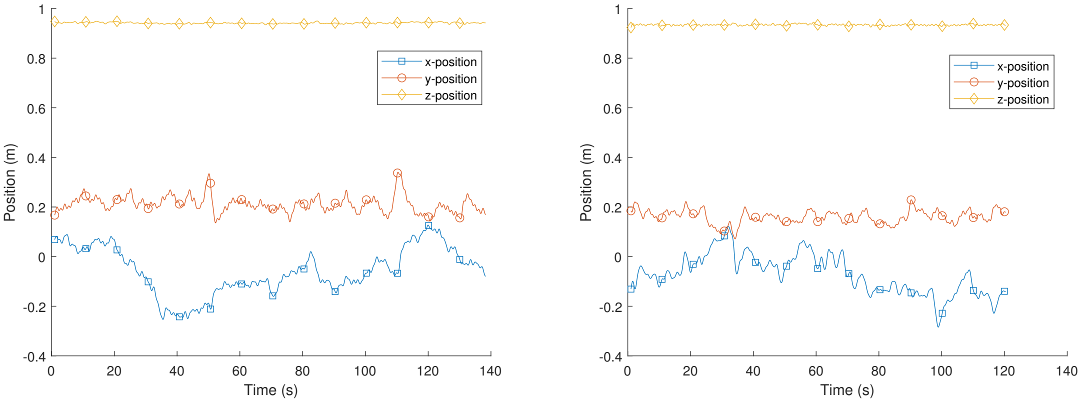

(e) Subject 5 (f) Subject 6

Fig. 16: Low filtered signal of the left hip marker, L_FMH, for each of the subjects. A minimal order low-pass filter with cutoff frequency of $\omega_{\mathrm{c}} = 0.5\,\mathrm{Hz}$ is used. It can be seen that only the drift is filtered here.

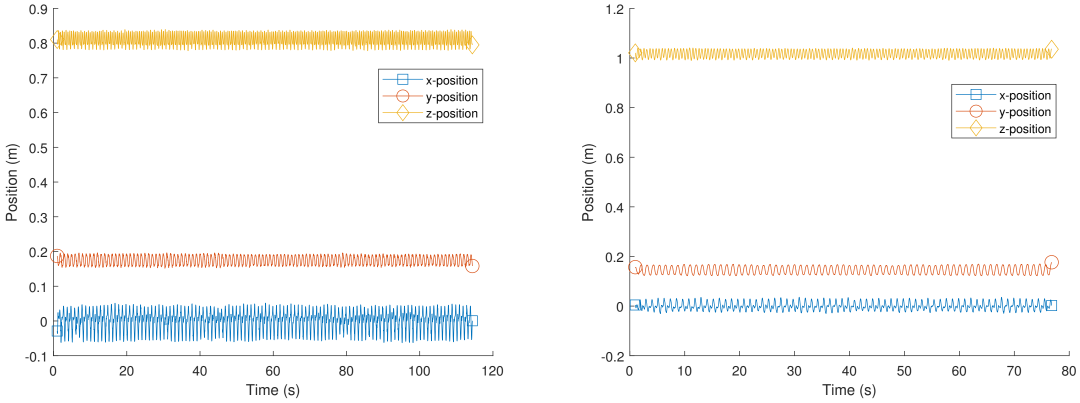

(a) Subject 1 (b) Subject 2

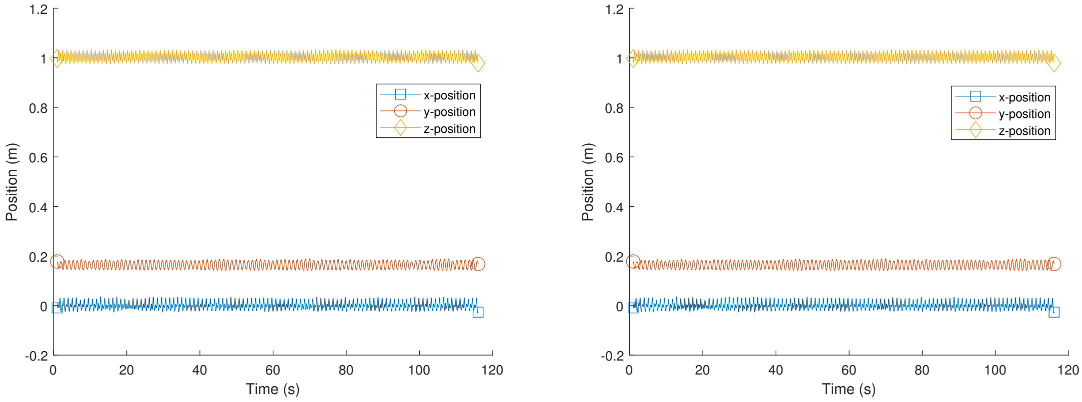

(c) Subject 3 (d) Subject 4

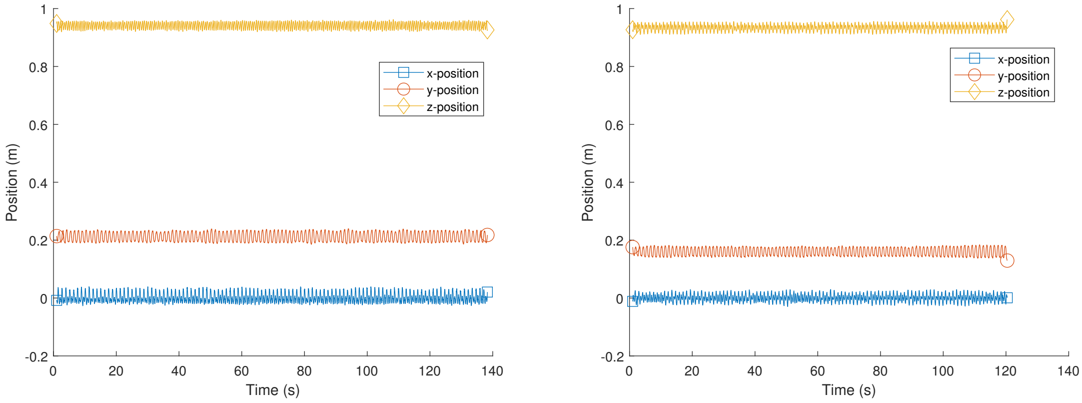

(e) Subject 5 (f) Subject 6

Fig. 17: Positions after subtracting the low filtered signal of the left hip marker, L_FMH, for each of the subjects. A minimal order low-pass filter with cutoff frequency of $\omega_c = 0.5\,\mathrm{Hz}$ is used. The steps are centered within MATE, however, while minimal at the hip, the steps still show some variation.

C: Finding the optimal design

Mapping forces in the tendon space $\vec{F}_\mathrm{t}$ to the Cartesian space $\vec{F}_\mathrm{R}$ and $\vec{F}_\mathrm{L}$ requires the Jacobian in Equation 6. This Jacobian relies on the inverse kinematics, i.e. it maps tendon movement to Cartesian movement. Obtaining this Jacobian requires the inverse relation between the end effector position in Cartesian coordinates $x, y,$ and z and the tendon lengths $L_1, L_2, L_3,$ and L_4. The definitions of these parameters are shown in Figure 18.Their relation also depends on the pulley positions $\vec{p}_1, \vec{p}_2, \vec{p}_3,$ and $\vec{p}_4$, which are also show in Figure 18. The inverse relation, i.e. the tendon lengths expressed in endpoint coordinates, are

$$L_1 = \sqrt{(p_{1,\mathrm{x}} - x)^2 + (p_{1,\mathrm{y}} - y)^2 + (p_{1,\mathrm{z}} - z)^2}, \tag{15}$$

$$L_2 = \sqrt{(p_{2,\mathrm{x}} - x)^2 + (p_{2,\mathrm{y}} - y)^2 + (p_{2,\mathrm{z}} - z)^2}, \tag{16}$$

$$L_3 = \sqrt{(p_{3,\mathrm{x}} - x)^2 + (p_{3,\mathrm{y}} - y)^2 + (p_{3,\mathrm{z}} - z)^2}, \tag{17}$$

$$L_4 = \sqrt{(p_{4,\mathrm{x}} - x)^2 + (p_{4,\mathrm{y}} - y)^2 + (p_{4,\mathrm{z}} - z)^2}. \tag{18}$$

The inverse kinematics can now be expressed in the required Jacobian by taking the partial derivative of these Equations to each cartesian coordinate, resulting in the Jacobian seen in Equation 6:

$$\mathbf{J}_\mathrm{t} = \begin{pmatrix} \frac{\partial L_1}{\partial x} & \frac{\partial L_1}{\partial y} & \frac{\partial L_1}{\partial z} \\ \frac{\partial L_2}{\partial x} & \frac{\partial L_2}{\partial y} & \frac{\partial L_2}{\partial z} \\ \frac{\partial L_3}{\partial x} & \frac{\partial L_3}{\partial y} & \frac{\partial L_3}{\partial z} \\ \frac{\partial L_4}{\partial x} & \frac{\partial L_4}{\partial y} & \frac{\partial L_4}{\partial z} \end{pmatrix}, \tag{6}$$

This Jacobian is used to map forces from the tendon space to the Cartesian space in Equations 4 and 5. The validity of these Equations can be checked using singular values, i.e. one Cartesian coordinate x and one tendon length L. This simplification gives the following Equations:

$$F_\mathrm{t}\dot{L} = F_\mathrm{x}\dot{x}, \tag{19}$$

$$F_\mathrm{t}\frac{\mathrm{d}L}{\mathrm{d}t} = F_\mathrm{x}\frac{\mathrm{d}x}{\mathrm{d}t}, \tag{20}$$

$$F_\mathrm{t}\frac{\partial L}{\partial x} = F_\mathrm{x}. \tag{21}$$

Here, Equation 21 is the singular value interpretation of Equations 4 and 5. Equation 19 holds because the power in both spaces should be equal.

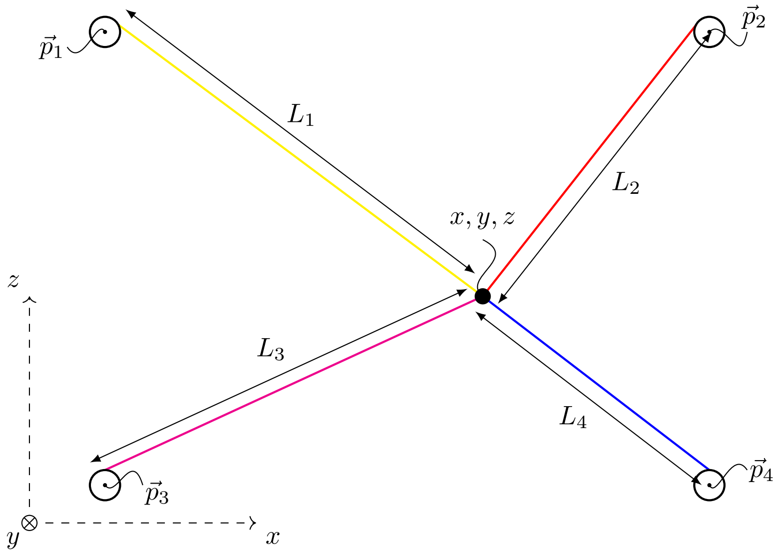

Fig. 18: Schematic view of the tendons attached to a single leg in the sagittal plane. The definitions for tendon lengths L_i, pulley positions $\vec{p}_i$ for tendon i, and Cartesian coordinates x, y, z at the robot end effector are shown here.

The stiffness is mapped from Cartesian space to tendon space using Equation 7. The validity of this Equation can also be shown using singular values. First, the inverse relation of Equation 21 is needed,

$$F_{\mathrm{t}} = \frac{\partial x}{\partial L} F_{\mathrm{x}}. \tag{22}$$

Now on both sides of the Equation the partial derivative to L is taken

$$\frac{\partial F_{\mathrm{t}}}{\partial L} = \frac{\partial x}{\partial L} \frac{\partial F_{\mathrm{x}}}{\partial L}. \tag{23}$$

Equation 21 is substituted back in:

$$\frac{\partial F_{\mathrm{t}}}{\partial L} = \frac{\partial x}{\partial L} \frac{\partial F_{\mathrm{x}}}{\partial x} \frac{\partial x}{\partial L}. \tag{24}$$

Here $\frac{\partial x}{\partial L}$ represents the inverse Jacobian from Equation 6 in singular values. Tendon stiffness is represented by $\frac{\partial F_{\mathrm{t}}}{\partial L}$, and Cartesian stiffness by $\frac{\partial F_{\mathrm{x}}}{\partial x}$. These terms represent the force with respect displacement, i.e. the stiffness. Equation 7 could potentially also be used to map a full stiffness Matrix in Cartesian space to the tendon space using a the inverse of the Jacobians in Equation 6 [29],

$$\mathbf{K_t} = \mathbf{J}_{\mathrm{t}}{}^{-T} \mathbf{K_x} \mathbf{J}_{\mathrm{t}}{}^{-1}. \tag{25}$$

Here a problem arises as the system is overactuated, i.e. the Jacobian matrix is not square. Therefore, it is impossible to calculate the inverse of the Jacobian matrix directly. Because only a singular stiffness in the x-direction is taken as reference stiffness, this problem is circumvented. However, future research might require the tendon stiffness to rely on a full stiffness matrix in Cartesian space. In this case, an additional optimization would be required to approximate the inverse of the Jacobian matrix.

Finding a suitable optimization algorithm is crucial for the validity of the final design. Multiple local minima in a system warrant the need to implement a global optimization. The combination of eight parameters for four configurations for six subjects means that the presence of multiple local minima somewhere in this optimization is highly likely. However, this should still be checked, as global optimizations are computationally expensive and are not guaranteed to find the global minimum [30]. Eight Parameters result in an eight-dimensional cost function, so a visual inspection of the entire cost function is difficult. Therefore, only one parameter is varied at a time while the other parameters are kept constant. Each parameter is varied from the lower to the upper bound, which is found in Table I. This parameter is then plotted against the cost function to check whether local minima are present. This process is repeated for each parameter, for each configuration, and each subject, giving a total of 192 graphs. All these graphs have been examined, but since all results are highly similar, only 16 typical graphs are included in this thesis.

The majority of the graphs are similar to the results seen in Figure 19, where the parameters are varied for subject two in combination with configuration four. Here only one minimum is present in each graph. However, this does not exclude the possibility of local minima, as the parameters are not varied against each other. Furthermore, as previously assumed, some local minima are observed during this examination. An example can be seen in Figure 20, where w_3 contains two minima. Two minima were detected in several of the graphs. Since this visualization only captures a small fraction of the possible combinations, it can be safely assumed that more local minima are present; thus, a global optimization method is required [30].

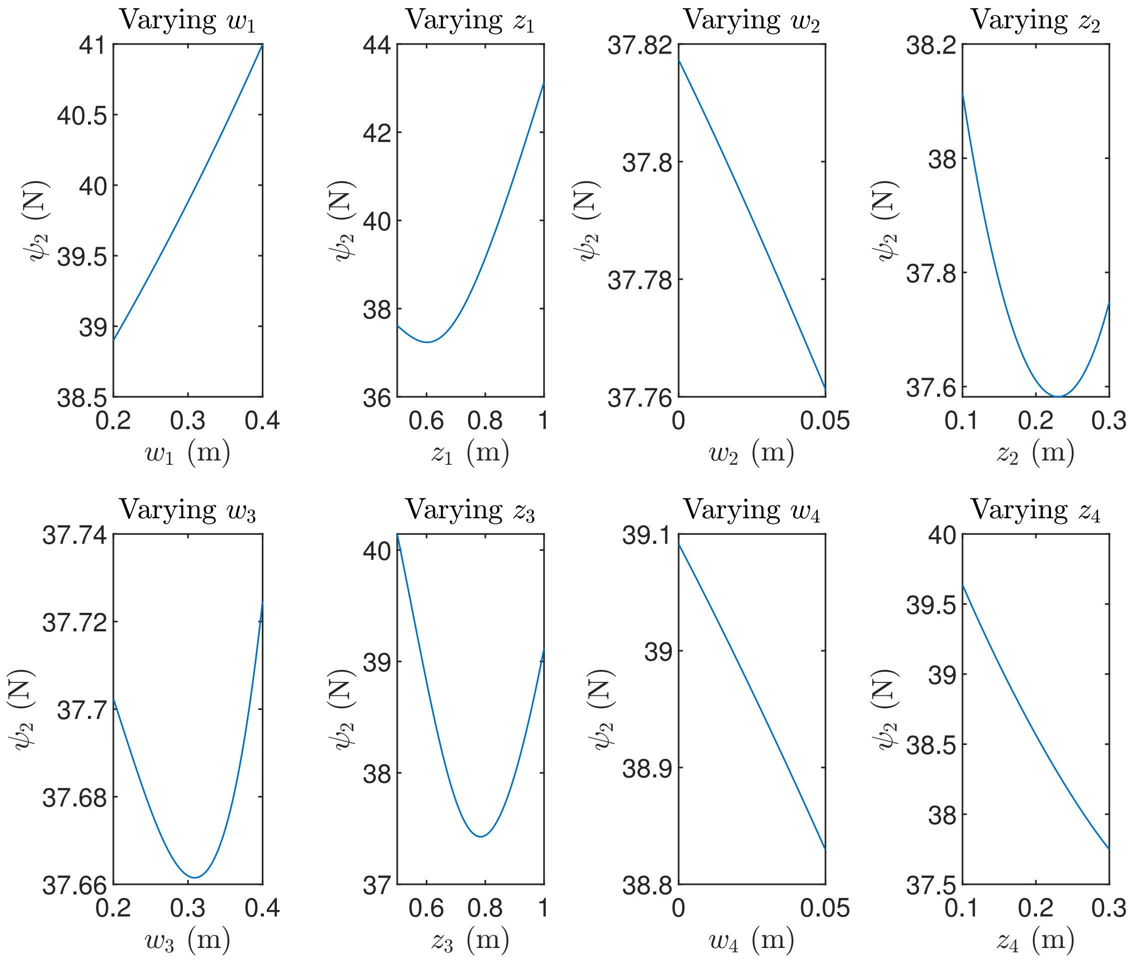

Fig. 19: Optimization parameters varied from the lower to the upper bound, represented against the cost function value. These specific results are for subject 2 and configuration 4, where only one minimum is visible in each graph.

A genetic algorithm is selected for the optimization, as it is a global method that can escape local minima due to mutations and evaluates multiple minima at once. The algorithm is run in MATLAB (R2021b, Mathworks). The algorithm is run five times for each configuration to increase the chances of finding the global minimum. Furthermore, an average cost function value of $1e-6$ over 100 generations is selected as the stopping criteria, and the optimization is visually inspected for large fluctuations in the cost function values.

The optimization is run five times on subjects in the selection group, i.e. subjects one, four, five, and six. The optimal parameter results are shown in Table III. The final cost function values are displayed in Table IV. A visualization of the optimal designs for all subjects can be found in Figures 21, 22, 23, and 24. Here it is again confirmed that all designs are relatively similar, with only some slight inter-subject variations. The design of subject one obtained the lowest mean cost function value via Equation 9, as can be found in Table IV.

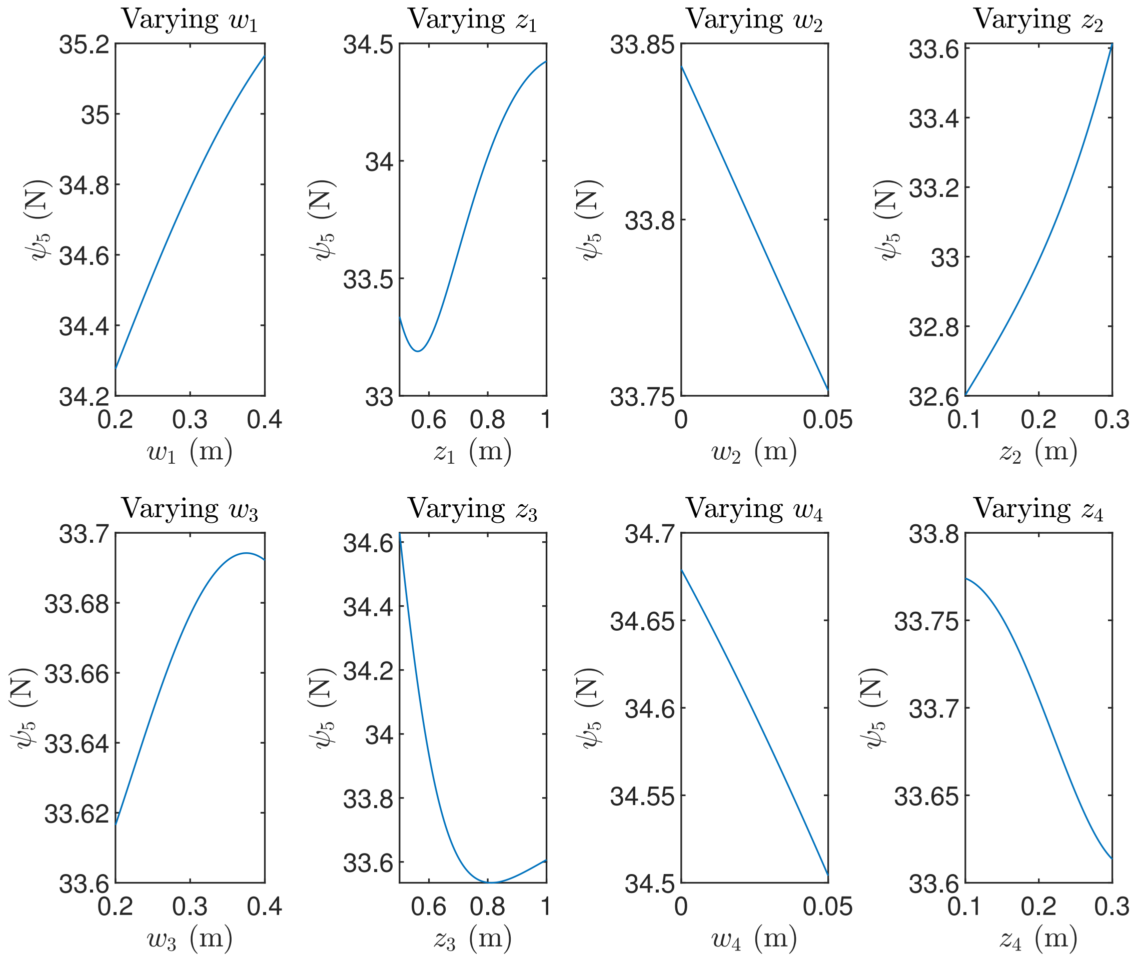

Fig. 20: Optimization parameters varied from the lower to the upper bound, represented against the cost function value. These specific results are for subject 5 and configuration 2, where a local minimum can be seen for w_3.

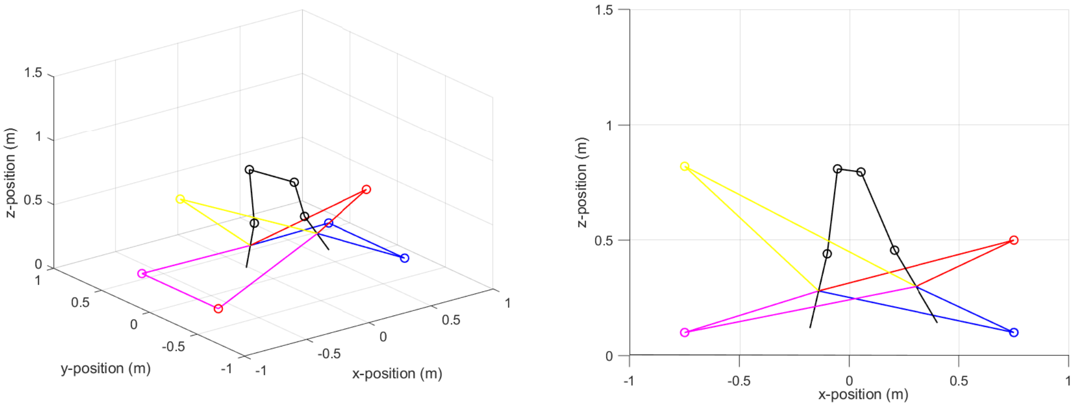

(a) Three dimensional view

(b) Side view

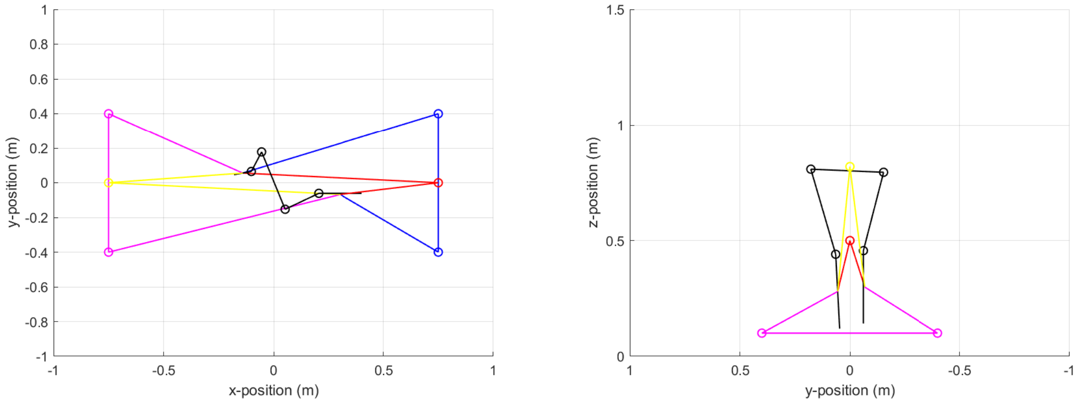

(c) Top view

(d) Back view

Fig. 21: The final optimal design found by the genetic algorithm for subject one. Configuration one is optimal for both the front and back. Views from all angles are included, to provide a clear overview of the design.

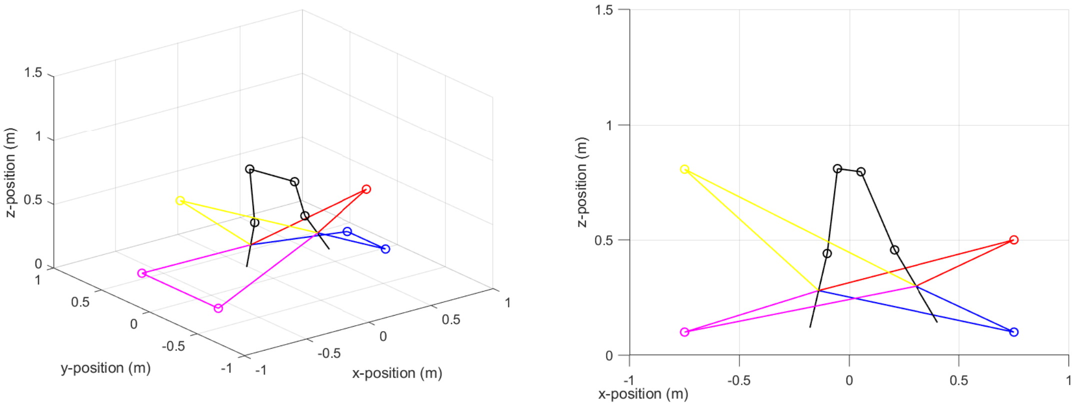

(a) Three dimensional view

(b) Side view

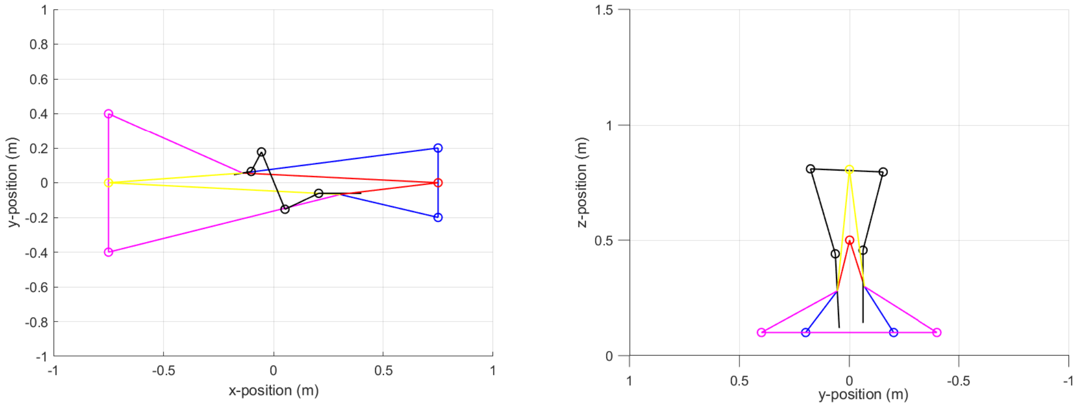

(c) Top view

(d) Back view

Fig. 22: The final optimal design found by the genetic algorithm for subject four. Configuration one is optimal for both the front and back. Views from all angles are included, to provide a clear overview of the design.

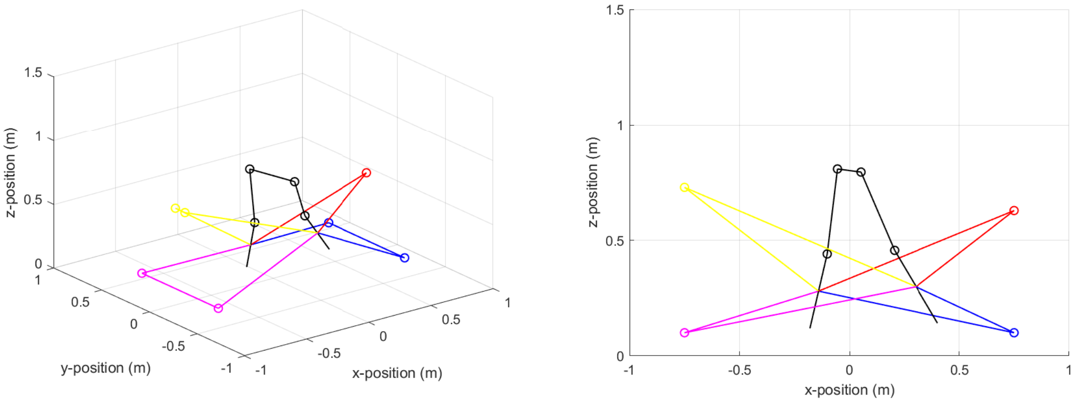

(a) Three dimensional view (b) Side view

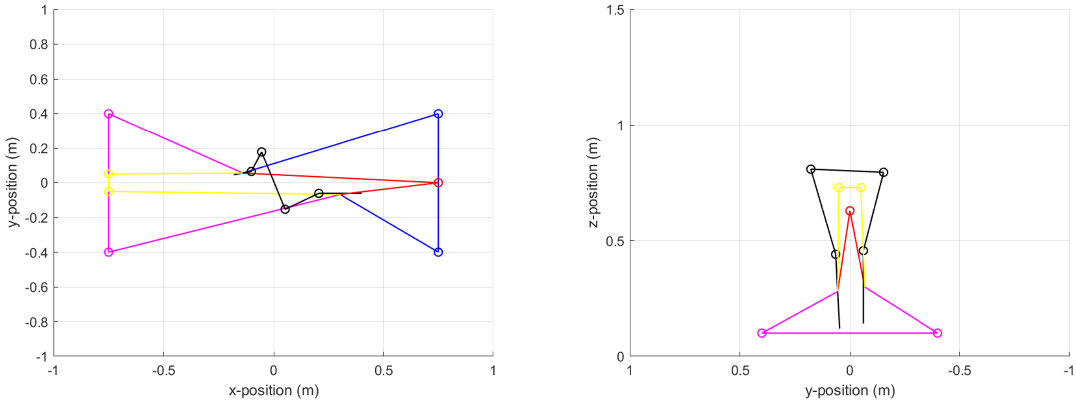

(c) Top view (d) Back view

Fig. 23: The final optimal design found by the genetic algorithm for subject five. Configuration one is optimal for both the front and back. Views from all angles are included, to provide a clear overview of the design.

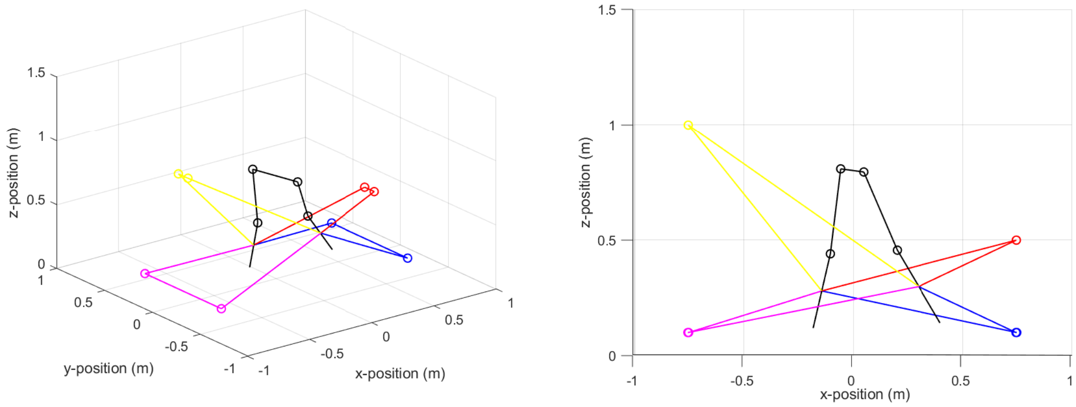

(a) Three dimensional view (b) Side view

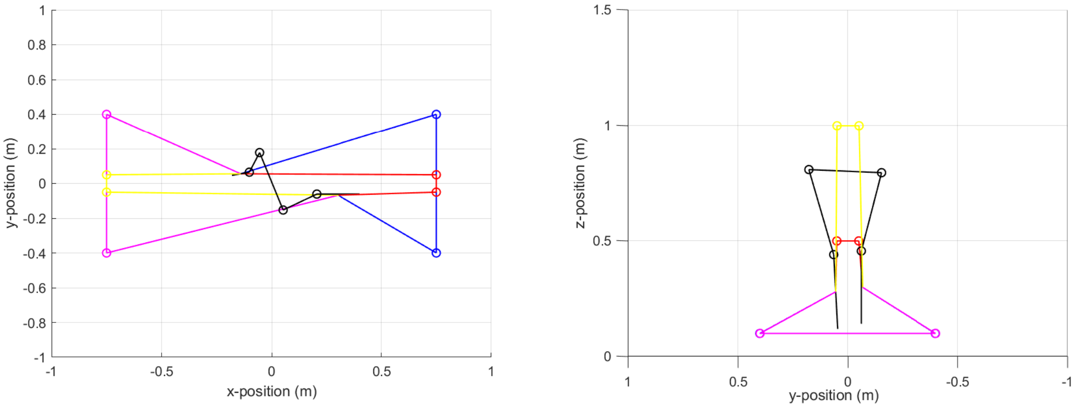

(c) Top view (d) Back view

Fig. 24: The final optimal design found by the genetic algorithm for subject six. Configuration one is optimal for both the front and back. Views from all angles are included, to provide a clear overview of the design.

D: Validation of the optimal design

Validation of the optimal design is done by evaluating the parasitic forces during healthy gait in both feet, in the Cartesian space. These forces are calculated with Equations 4 and 5. After this, they are mass normalized to the bodyweight m_j of each Subject j, i.e.

$$\hat{\mathbf{F}}_{\mathrm{L},j} = \frac{\mathbf{F}_{\mathrm{L}}}{m_j}, \tag{26}$$

$$\hat{\mathbf{F}}_{\mathrm{R},j} = \frac{\mathbf{F}_{\mathrm{R}}}{m_j}. \tag{27}$$

These forces are calculated for subjects in the validation group, i.e. subject two and three, when using the optimal design. The results over the full 10 steps can be seen in Figure 25 for subject two and Figure 26 for subject three. Interestingly, the forces in both the left and right legs look very similar. Intuitively this makes sense, as the tendons are connecting both legs. Elongation of the tendon will thus produce the same tendon force $\mathbf{F}_{\mathrm{t}}$ on both legs, with the only difference being the position of the legs. The forces are largest in the x-direction, or sagittal plane, in the forward and backward direction. This also makes sense, as the tendons are mainly pointing in this direction.

The validation threshold are visualized in Figure 27 and 28 for subject two and three respectively. They are calculated using Equations 10 and 11, using leg velocity. This leg velocity $\mathbf{v}$ is numerically approximated in MATLAB based on the available marker position data $\vec{q}$, by computing

$$\mathbf{v} = \frac{\mathrm{d}\vec{q}}{\mathrm{d}t}, \tag{28}$$

where timestep $\mathrm{d}t$ is determined by sampling rate f_{s}:

$$\mathrm{d}t = \frac{1}{fs} = \frac{1}{100\,\mathrm{Hz}} = 0.01\,\mathrm{s}. \tag{29}$$

Since numerical approximations like this are noisy, the velocity is processed with a moving average over a window of five time steps. This process smooths the velocity making it a more realistic approximation of the real velocities. In both threshold plots in Figure 27 and 28 the left and right leg move asymmetrically, in contrast to the forces. This finding makes sense since one leg is in the swing phase while the other is in the stance phase. Combining this with double the amount of peaks for parasitic forces makes it very difficult to validate the results. Furthermore, it can be observed that the forces are at least twice as high as the thresholds. The parasitic forces do not lie within the validation threshold and thus potentially pose a danger of altering the step length of subjects using MATE.

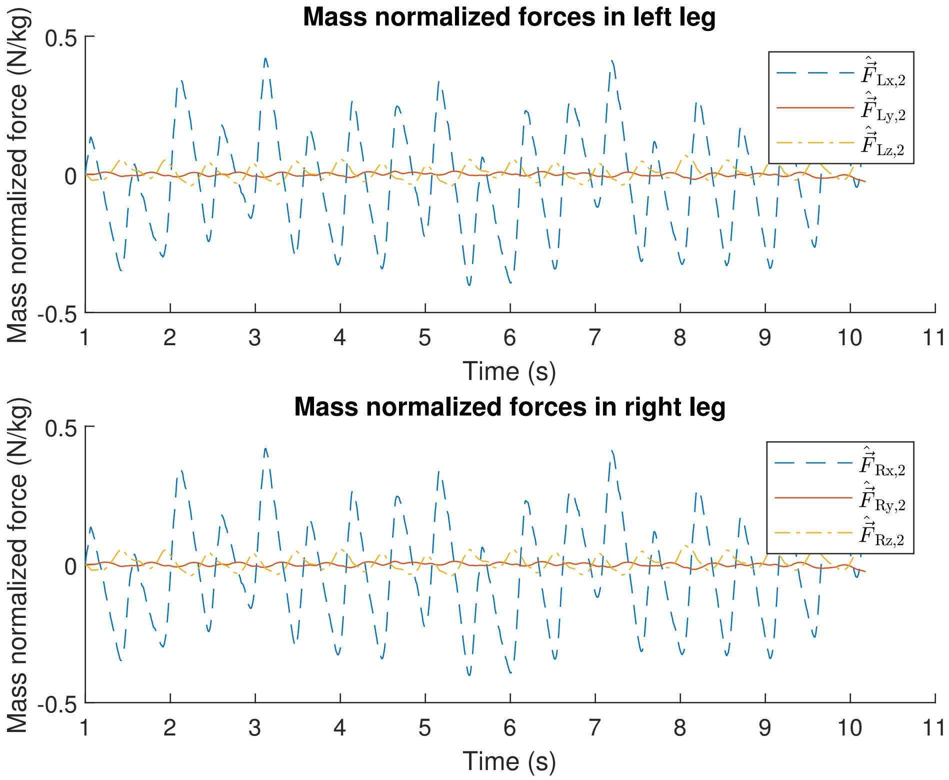

Fig. 25: Mass normalized parasitic forces acting on the left and right leg of Subject two when using the optimal configuration. Both the left and right leg are shown, with forces in the Cartesian space.

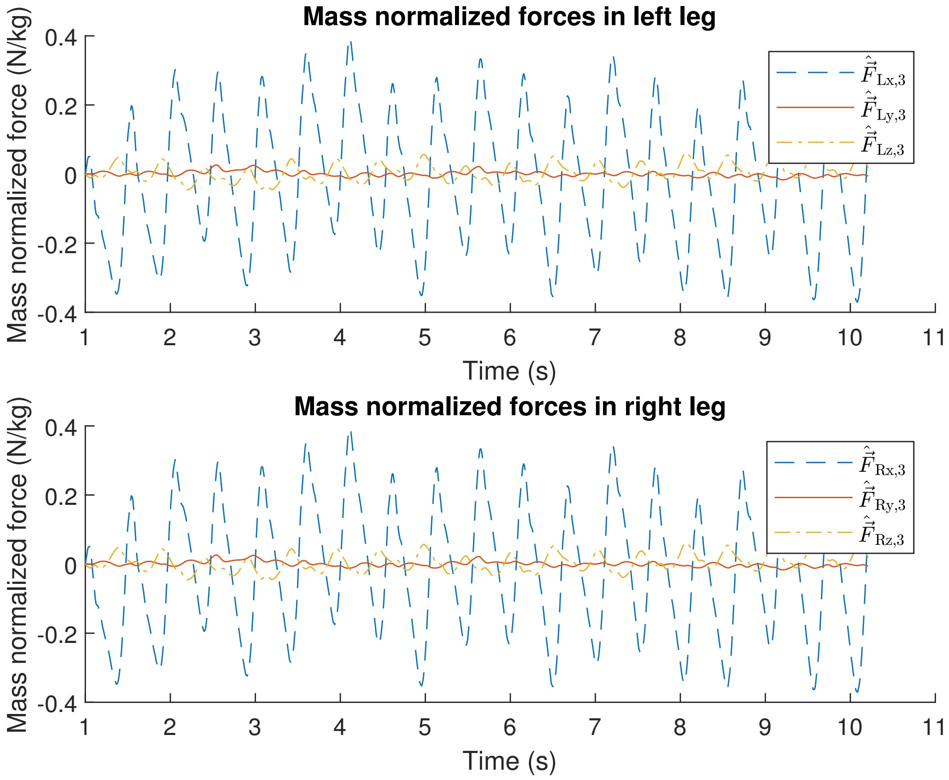

Fig. 26: Mass normalized parasitic forces acting on the left and right leg of Subject three when using the optimal configuration. Both the left and right leg are shown, with forces in the Cartesian space.

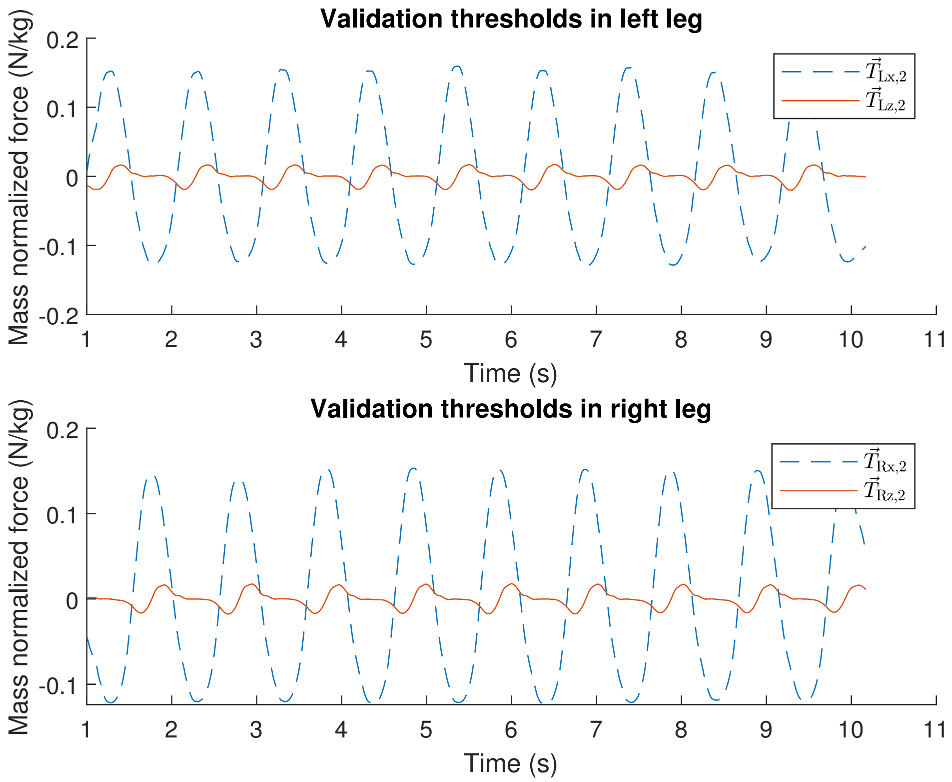

Fig. 27: Validation threshold for subject two over all 10 steps. The validation threshold is chosen as these values produce a 30% increase in step length.

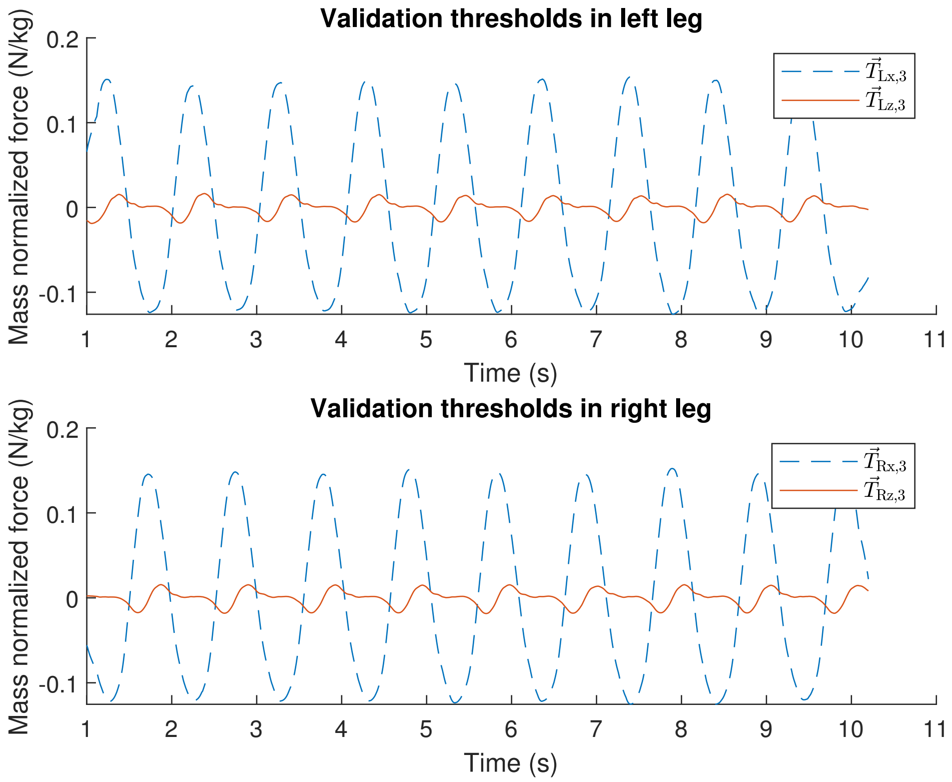

Fig. 28: Validation threshold for subject three over all 10 steps. The validation threshold is chosen as these values produce a 30% increase in step length.